

# Statistical Inferences and Predictions for Areal Data and Spatial Data Fusion with Hausdorff–Gaussian Processes

Lucas da Cunha Godoy

Department of Statistics, University of Connecticut

Marcos Oliveira Prates

Department of Statistics, Universidade Federal de Minas Gerais

Jun Yan

Department of Statistics, University of Connecticut

August 2, 2024

## Abstract

Accurate modeling of spatial dependence is pivotal in analyzing spatial data, influencing parameter estimation and out-of-sample predictions. The spatial structure and geometry of the data significantly impact valid statistical inference. Existing models for areal data often rely on adjacency matrices, struggling to differentiate between polygons of varying sizes and shapes. Conversely, data fusion models, while effective, rely on computationally intensive numerical integrals, presenting challenges for moderately large datasets. In response to these issues, we propose the Hausdorff-Gaussian process (HGP), a versatile model class utilizing the Hausdorff distance to capture spatial dependence in both point and areal data. We introduce a valid correlation function within the HGP framework, accommodating diverse modeling techniques, including geostatistical and areal models. Integration into generalized linear mixed-effects models enhances its applicability, particularly in addressing change of support and data fusion challenges. We validate our approach through a comprehensive simulation study and application to two real-world scenarios: one involving areal data and another demonstrating its effectiveness in data fusion. The results suggest that the HGP is competitive with specialized models regarding goodness-of-fit and prediction performances. In summary, the HGP offers a flexible and robust solution for modeling spatial data of various types and shapes, with potential applications spanning fields such as public health and climate science.

*Keywords:* Areal data, CAR models, Geostatistics, Spatial modeling, Spatial prediction

# 1 Introduction

Accounting for spatial dependence is pivotal in spatial data analysis. Valid statistical inference are deeply influenced by the spatial structure and geometry of the data. Point-referenced data are typically analyzed using geostatistics methods (e.g., [Cressie, 1993](#)). For areal data, the conditional autoregressive model (CAR) ([Besag, 1974](#)) and its variants ([Besag et al., 1991](#); [Rodrigues and Assunção, 2012](#); [Datta et al., 2019](#); [Cruz-Reyes et al., 2023](#)) are often preferred. The nature of the observed spatial data significantly influences the choice of statistical methodology. This becomes increasingly critical in complex inferential problems, such as predicting a variable in a target map using data from a source map. This issue, known as change of support ([Cressie, 1993](#), pg. 284–289), requires tailored methods depending on the spatial units involved ([Gelfand et al., 2001](#)). Spatial data from diverse sources often differ in spatial units or supports, resulting in spatial misalignment ([Gotway and Young, 2002](#)). Data fusion is necessitated when a spatial variable is provided by multiple, potentially misaligned, sources ([Moraga et al., 2017](#)).

Both traditional areal models and data fusion models for spatial data exhibit inherent limitations. Traditional areal models face challenges with predictions for overlapping spatial units ([Bakar and Jin, 2020](#)), do not account for region size or shape of the areal units and lack interpretable spatial dependence parameters ([Assunção and Krainski, 2009](#); [Cruz-Reyes et al., 2023](#)). An exception of the last limitation is the directed acyclic graph autoregressive (DAGAR) model, which offers an interpretable parameter ([Datta et al., 2019](#)). Data fusion models, which view areal data as averages of a continuous process, may be unsuitable for discrete outcomes ([Gelfand et al., 2001](#)). Additionally, their reliance on arbitrary discretization for likelihood evaluation lacks consensus on optimal resolution ([Fuentes and Raftery, 2005](#); [Liu et al., 2011](#); [Wang and Furrer, 2021](#)) and can introduce unquantifiable biases ([Gonçalves and Gamerman, 2018](#)).

We propose a unified approach for analyzing spatial data encompassing areal, point-referenced, and mixed spatial supports. This methodology combines Gaussian processes (GPs)

with the Hausdorff distance (Shephard and Webster, 1965). The Hausdorff distance, defined on a reference metric space, effectively measures between the distance between two sets while accounting for their shape and size. For point pairs, it reduces to the distance metric associated to the reference metric space. GPs, recognized for their flexibility, are widely utilized in spatial data modeling, notably as priors in generalized mixed effects models (Diggle et al., 1998), for spatially varying regression coefficients (Gelfand et al., 2003), and in addressing spatial misalignment issues (Banerjee and Gelfand, 2002). The Hausdorff–Gaussian process (HGP) that we propose is a GP with a correlation function defined on the Hausdorff distance between sample units, allowing integrating their shape and size into the analysis. With some assurance of positiveness definiteness of the resulting covariance matrix, the HGP with a powered exponential correlation can be used in place of GPs to adeptly model areal, point-referenced, and mixed spatial data types, offering a new avenue in analyzing spatial and spatiotemporal data with mixed supports.

This paper is structured as follows. Section 2 introduces the Hausdorff distance, discussing its properties, and then delineates the HGP, highlighting its significant applications. Section 3 sets up spatial generalized linear mixed models (GLMM) with HGP components and details their inferences in the Bayesian framework. A simulation study to compare the proposed model with specific models for areal and fused data is presented in Section 4. Section 5 demonstrates the practical utility of our model through two distinct applications, one on areal data and the other on data fusion. Section 6 concludes with a discussion.

## 2 Hausdorff–Gaussian Process

### 2.1 Hausdorff Distance

The Hausdorff distance is a metric measuring the distance between two sets of points. Specifically, it is the greatest distance from a point in one set to the closest point in the other set. Consider a metric space  $(D, d)$ , where  $D$  is a spatial region of interest and  $d(x, y)$  defines

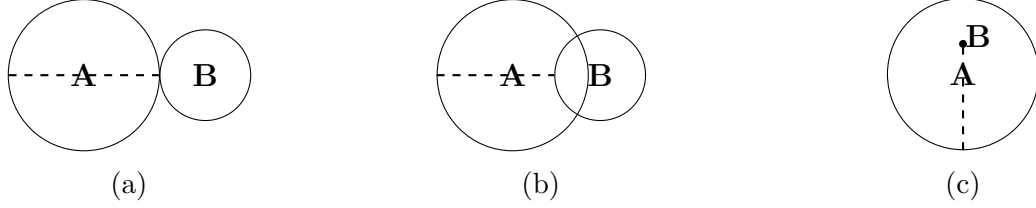


Figure 1: Three different pairs of bounded subsets of the Euclidean plane. In (a) the sets  $A$  and  $B$  share a single point on their border. In (b), they have non-empty intersection. While in (c),  $B$  is a singleton set contained by  $A$ . The dashed lines represent the Hausdorff distance between the sets.

the distance between any two elements  $x, y \in D$ . For a single point  $x$  and a set  $A$ , define  $d(x, A) = \inf_{a \in A} d(x, a)$  as the closest distance from  $x$  to any element in  $A$ . The directed Hausdorff distance from a set  $A$  to a set  $B$  is  $\vec{h}(A, B) = \sup_{a \in A} d(a, B)$ . This measure is not necessarily symmetric. The symmetric Hausdorff distance is defined as the greater of the two directed Hausdorff distances:  $h(A, B) = \max \left\{ \vec{h}(A, B), \vec{h}(B, A) \right\}$ . Note that if  $A$  and  $B$  are both singletons, then  $h(A, B) = d(A, B)$ .

In spatial analysis, the Hausdorff distance provides a robust and suitable metric over non-empty, bounded, and compact subsets of  $D$ , denoted as  $\mathcal{B}(D)$  (Sendov, 2004). While not functioning as a conventional distance in unbounded sets, it is highly effective in bounded contexts, which are prevalent in spatial statistics. Typically, the study region  $D$  in spatial statistics is a bounded subset of  $\mathbb{R}^2$ , where the Hausdorff distance excels in quantifying distances between spatial units by capturing both their shapes and sizes.

To demonstrate the efficacy of the Hausdorff distance in measuring distances between various spatial units, Figure 1 presents three simple examples. In each sub-figure, set  $A$  is represented as a circle with a radius of 1. Figure 1a introduces a set  $B$ , a circle tangent to  $A$ . Figure 1b examines the distance between two sets having a non-empty intersection. Figure 1c features  $B$  as an interior point of  $A$ . The dashed lines in the figures delineate the Hausdorff distances between the sets, highlighting the metric's ability to consider the shape, size, and orientation of the objects. This contrasts with other simpler distance functions between non-empty sets, such as the infimum distance between two sets, denoted  $\inf_{x \in X} \inf_{y \in Y} d(x, y)$ .

This distance does not fulfill the metric property of positiveness condition. In other words,  $d(x, y) = 0$  does not imply  $x = y$ . Indeed, employing such distance latter would yield a distance of zero between the three pairs of sets depicted in Figure 1.

## 2.2 Hausdorff–Gaussian Process

HGP is a natural extension of GP for modeling spatial data defined on the Hausdorff distance. A GP is a stochastic process over an index set such that all its finite-dimensional marginal distributions are multivariate normal distributions. An HGP expands the index set on a spatial region  $D$  to encompasses a broader range of spatial units,  $\mathcal{B}(D)$ , which contains non-empty, bounded, and compact subsets of  $D$ . To define an isotropic HGP  $Z(\cdot)$  over  $\mathcal{B}(D)$ , we specify a marginal mean function function  $m(\cdot)$ , a positive-valued marginal standard deviation (SD) function  $v(\cdot)$ , and an isotropic correlation function  $r(h)$  for any two sets apart in Hausdorff distance  $h$ . With these functions, an HGP over  $\mathcal{B}(D)$  is a stochastic process  $Z(\cdot)$  whose marginal distribution at  $\mathbf{s}_1, \dots, \mathbf{s}_p \in \mathcal{B}(D)$  is multivariate normal with mean vector and covariance matrix, respectively,

$$\mathbb{E}[Z(\mathbf{s}_i)] = m(\mathbf{s}_i) \quad \text{and} \quad \text{Cov}[Z(\mathbf{s}_i), Z(\mathbf{s}_j)] = v(\mathbf{s}_i)v(\mathbf{s}_j)r(h(\mathbf{s}_i, \mathbf{s}_j)), \quad (1)$$

for  $i, j = 1, \dots, p$ , where  $h(\mathbf{s}_i, \mathbf{s}_j)$  is the Hausdorff distance between  $\mathbf{s}_i$  and  $\mathbf{s}_j$ . This process allows for representations of diverse spatial data, from areal to mixed, making it suitable for a wide range of applications such as disease mapping and data fusion.

Denote the HGP process defined in Equation (1) by  $\text{HGP}\{m(\cdot), v(\cdot), r(\cdot)\}$ . The mean function  $m(\cdot)$  captures large-scale variations, usually through covariates. The SD function  $v(\cdot)$  function accommodates both homoscedastic and hereroscedastic scenarios. For instance, with a log link and covariate  $w(\mathbf{s})$  at spatial unit  $\mathbf{s}$ , a natural model is

$$\log v(\mathbf{s}) = \alpha_0 + \alpha_1 w(\mathbf{s}). \quad (2)$$

Equation (2) allows a distinction between point-referenced and areal data, a need in data fusion applications (Wang and Furrer, 2021). With  $\mathcal{A}(\cdot)$  being the function that returns the area of a spatial object. A covariate  $w(\mathbf{s}) = \mathbb{1}(\mathcal{A}(\mathbf{s}) > 0)$  enables different variances between these data types. Certainly, care is necessary in specifying  $v(\mathbf{s})$  to ensure a valid GP (Palacios and Steel, 2006).

## 2.3 Correlation Function

The correlation function  $r(\cdot)$  needs to be carefully chosen to ensure the validity of the HGP as it defines the spatial dependence structure across different locations. In particular, we focus on isotropic correlation functions. Therefore, unless explicitly mentioned, all subsequent references to correlation functions will assume they are isotropic. A valid correlation function must be positive definite and meet two key criteria:  $r(0) = 1$  and  $\lim_{h \rightarrow \infty} r(h) = 0$  (Cressie, 1993, Ch. 2.3.2), where  $h$  is the Hausdorff distance between a pair  $\mathbf{s}, \mathbf{s}' \in \mathcal{B}(D)$ . The latter ensures that spatial correlation diminishes with increasing distance. It is noteworthy that while most geostatistical correlation functions are constructed for Euclidean spaces (Cressie, 1993, Ch. 2.5.1), their positive definiteness may not extend to non-Euclidean spaces (Curriero, 2006; Li et al., 2023). This raises the question of whether existing frameworks can be adapted or if entirely new formulations are needed to maintain the mathematical rigor in non-Euclidean settings.

For practical purposes, we propose to use a two-parameter powered exponential correlation (PEC) function

$$r(h; \varphi, \nu) = \exp \left\{ -\frac{h^\nu}{\varphi^\nu} \right\},$$

where  $\nu$  controls the smoothness and  $\varphi$  governs the range of the spatial dependence. To enhance interpretability, we reparametrize this function with  $\rho = \log(10)^{1/\nu} \varphi$ . Consequently,  $\rho$  is the distance at which the spatial correlation between a pair of spatial units drops to 0.10, commonly referred to as the practical range. The PEC function is appealing because

the following Proposition 2.1 guarantees its positive definiteness for  $\nu \in (1/2, 1)$ . The proof of the proposition is based on probabilistic embedding of Hausdorff metrics (Backurs and Sidiropoulos, 2016).

**Proposition 2.1.** *Let  $h = h(\mathbf{s}, \mathbf{s}')$  be the Hausdorff distance between two spatial units, denoted  $\mathbf{s}, \mathbf{s}' \in \mathcal{B}(D)$ , where  $D \subset \mathbb{R}^2$ . The powered exponential correlation function  $\exp\{-h^\nu/\varphi^\nu\}$  is positive definite for  $\nu \in (1/2, 1)$ .*

In addition to the theoretical result, an empirical assessment was used to provide evidence for the positive definiteness of this function for an expanded range of  $\nu \in (0, 1)$ . The positive definiteness is satisfied for bigger  $\nu$  values when the dependence range  $\rho$  is smaller. See details in Section B of the appendix.

## 3 HGP in Spatial GLMM

### 3.1 Model

Generalized linear models for spatial data can benefit from replacing the GP with the HGP as spatial random effects. In this context, assume  $\mathcal{S} = \{\mathbf{s}_1, \dots, \mathbf{s}_n\}$  is a set of spatial units or locations such that  $\mathbf{s}_i \in \mathcal{B}(D)$ , where  $D \subset \mathbb{R}^2$ . Consider a response variable  $Y(\mathbf{s}_i)$  and a  $p$ -dimensional vector of covariates  $\mathbf{X}_i$  associated to the  $i$ -th spatial unit. Let  $\mathbf{Z} = [Z(\mathbf{s}_1), \dots, Z(\mathbf{s}_n)]^\top$  be an  $n$ -dimensional vector of latent spatial random effects. Conditional on  $Z(\mathbf{s}_i)$  and  $\mathbf{X}_i$ , we assume that the responses  $Y(\mathbf{s}_i)$ 's are mutually independent. The conditional distribution of  $Y(\mathbf{s}_i)$  is characterized by its mean and possibly some additional parameters. This leads to a spatial GLMM built on an HGP.

Specifically, the spatial GLMM is specified as

$$Y(\mathbf{s}_i) \mid \mathbf{X}_i, Z(\mathbf{s}_i) \stackrel{\text{ind}}{\sim} f(\cdot \mid \mu_i, \boldsymbol{\gamma}), \quad (3)$$

where  $f(\cdot \mid \mu_i, \boldsymbol{\gamma})$  is a probability density or mass function of a distribution with expectation

$\mu_i$  and an additional parameter vector  $\boldsymbol{\gamma}$ . The conditional mean  $\mu_i$  is linked to the covariate vector and the spatial random effects through a suitable, known link function  $g$ :

$$\mu_i = \mathbb{E}[Y(\mathbf{s}_i) \mid \mathbf{X}_i, Z(\mathbf{s}_i)] = g^{-1}(\mathbf{X}_i^\top \boldsymbol{\beta} + Z(\mathbf{s}_i)), \quad (4)$$

where  $\boldsymbol{\beta}$  is a  $p$ -dimensional regression coefficient vector. The spatial dependence among the responses  $\mathbf{Y} = [Y(\mathbf{s}_1), \dots, Y(\mathbf{s}_n)]^\top$  is introduced by an HGP on  $\mathbf{Z}$ , namely,

$$\mathbf{Z} \sim \text{HGP}\{0, v(\cdot; \boldsymbol{\sigma}), r(\cdot; \boldsymbol{\delta})\}, \quad (5)$$

with zero-mean, a SD function  $v(\cdot; \boldsymbol{\sigma})$  with parameters  $\boldsymbol{\sigma}$ , and the PEC function  $r(\cdot, \boldsymbol{\delta})$  with parameters  $\boldsymbol{\delta} = \{\rho, \nu\}$ . To summarize, the parameters of the spatial GLMM are  $\boldsymbol{\theta} = \{\boldsymbol{\beta}^\top, \boldsymbol{\sigma}^\top, \boldsymbol{\delta}^\top, \boldsymbol{\gamma}^\top\}^\top$ .

A general spatial GLMM is obtained by choosing a suitable  $f(\cdot \mid \mu_i, \boldsymbol{\gamma})$  for the response. For binary response variables, a Bernoulli distribution yields a spatial logistic regression. Count data can be modeled with either a Poisson or Negative Binomial distribution, depending on the presence of overdispersion. When the conditional distribution of the response is normal, the additional parameter  $\boldsymbol{\gamma}$  is the measurement error or small scale variance parameter. Let  $\mathbf{X}$  be a  $n \times p$  matrix with its  $i$ -th row given by  $\mathbf{X}_i$ . From the conditional dependence, the joint density (or mass) function of  $\mathbf{Y}$  conditioning on  $\mathbf{X}$  and  $\mathbf{Z}$  is

$$p(\mathbf{y} \mid \mathbf{X}, \mathbf{z}) = \prod_{i=1}^n f(y(\mathbf{s}_i) \mid \mu_i, \boldsymbol{\gamma}), \quad (6)$$

where  $\mathbf{y}$  and  $\mathbf{z}$  are realizations of  $\mathbf{Y}$  and  $\mathbf{Z}$ , respectively.

## 3.2 Bayesian Inferences

Prior distributions for all the model parameters are to be specified to complete the Bayesian model specification. For fixed effects regression coefficients ( $\boldsymbol{\beta}$ ), we employ uncorrelated zero-

mean Normal priors with marginal variances  $10^2$ . In the homoscedastic case, on  $\sigma$  we place a half-t prior with 3 degrees of freedom, denoted  $t_+(3)$  (Gelman, 2006). For the heteroscedastic model (2), we set independent standard normal priors for  $\alpha_0$  and  $\alpha_1$ . The PEC dependence is encoded through  $\boldsymbol{\delta} = \{\rho, \nu\}$ . In geostatistics, smoothness parameters for correlation functions are typically fixed, and their estimation properties are rarely reported (Zhang, 2004). Due to this and the scope of this paper, we specify separate models for different values of  $\nu$  ensuring a positive definite PEC and select the best fit for inference. The spatial dependence parameter  $\rho$  is also inherently difficult. Thus, to avoid oversmoothing, we employ an exponential prior for  $\rho$  with mean  $\lambda_\rho = -\rho_0/\log(p_\rho)$ , where  $\rho_0$  is an upper-bound set to four-fifths of the largest observed Hausdorff distance, and  $p_\rho$  is the probability that  $\rho$  exceeds  $\rho_0$ . The resulting prior concentrates its mass on lower values  $\rho$ .

The posterior distribution of  $\boldsymbol{\theta}$  and  $\mathbf{Z}$  given the observed data  $\mathbf{y}$  and  $\mathbf{X}$  is

$$\pi(\boldsymbol{\theta}, \mathbf{z} \mid \mathbf{y}) \propto p(\mathbf{y} \mid \mathbf{X}, \mathbf{z}, \boldsymbol{\beta}, \boldsymbol{\gamma})\pi(\mathbf{z} \mid \boldsymbol{\sigma}, \boldsymbol{\delta})\pi(\boldsymbol{\theta}), \quad (7)$$

where  $\pi(\cdot)$  denotes prior and posterior distributions of its arguments. Importantly, the distribution placed on the random effects  $\mathbf{z}$  also functions as a prior, as we draw samples from these latent effects distribution conditioned on the observed data.

**Parameter Estimation** The estimation of the spatial GLMM parameters is obtained from the posterior distribution defined in Equation (7). As the posterior distribution is intractable, we use the No-U-Turn (Hoffman and Gelman, 2014) Markov Chain Monte Carlo (MCMC) sampler available in Stan (Team, 2023) to draw samples from it. The No-U-Turn algorithm samples all the model parameters jointly and efficiently exploits the parameter space using automatic differentiation. Additionally, it eliminates the need for hand-tuning, making it a highly convenient sampler. We initialize the parameters with samples from their respective prior distributions. The latent random effects are initialized from a standard Gaussian distribution. The number of samples and the warm-up period of the MCMC algorithm

are application dependent. We assess the convergence of the chains using the split- $\hat{R}$  diagnostic (Vehtari et al., 2021). Finally, the parameters' point estimates and 95% credible intervals (CI) are obtained as, respectively, the median and percentiles (2.5 and 97.5, unless otherwise stated) of the marginal MCMC samples.

**Model Comparison** The assessment of goodness-of-fit (GoF) in the simulation study and applications involved two model comparison criteria: the leave-one-out information criterion (Vehtari et al., 2017, LOOIC), and the widely applicable information criterion (Watanabe, 2010, WAIC). For both of them, lower values indicate a better fit. We did not use the deviance information criterion due to its assumption of a small number of parameters relative to the sample size (McElreath, 2016, Ch. 7.4), which would require computationally intensive numerical integration of random effects in some of our models. When comparing a single candidate model to the HGP, we utilize the difference in the GoF metric  $G$  between the HGP and the given model, denoted by  $\Delta_G$ . Consequently, a negative  $\Delta_G$  suggests that the HGP model is a better fit for the data. The competing methods depend on the type of application we are working with and will be mentioned in the upcoming sections.

**Predictions** Predicting spatial phenomena accurately at unobserved locations is crucial in many applications, especially in change of support settings (Gelfand et al., 2001). The HGP prior for spatial random effects in GLMMs offers a powerful solution. For a set of  $m$  unobserved locations  $\mathcal{S}^* = \{\mathbf{s}_1^*, \dots, \mathbf{s}_m^*\}$ , we define an  $m$ -dimensional variable  $\mathbf{Y}^*$  representing the response variable at these locations. Assuming covariates from Equation (4) are available, we can generate predictions accounting for uncertainty using the posterior predictive distribution of  $\mathbf{Y}^*$ :

$$p(\mathbf{y}^* | \mathbf{y}) = \int p(\mathbf{y}^* | \mathbf{z}^*, \boldsymbol{\theta})p(\mathbf{z}^* | \mathbf{z}, \boldsymbol{\theta})\pi(\boldsymbol{\theta} | \mathbf{y})d\boldsymbol{\theta}, \quad (8)$$

where  $\mathbf{z}^* = (z(\mathbf{s}_1^*), \dots, z(\mathbf{s}_m^*))^\top$  is a realization of the spatial random effect at the new locations, and  $\boldsymbol{\theta}$  represents the model parameters. Details on sampling from this distribution are provided in Section C of the appendix.

## 4 Simulation Studies

### 4.1 Areal Data

We conducted a simulation study to assess the performance of the HGP relative to the DAGAR model, a state-of-the-art model designed explicitly for areal data (Datta et al., 2019), in modeling data generated from other models. We grounded our simulations in a real-world context by utilizing the 134 Intermediate Zones (IZ) north of the River Clyde within the Greater Glasgow in Scotland (Figure A.8), mirroring the application detailed in the upcoming Section 5.1. This region exhibits a range of Hausdorff distances between zones, from 0.7 to 37.7 kilometers (median: 9.4 km). Data were generated under a Poisson GLMM with a log link function, incorporating a single explanatory variable drawn from a standard normal distribution. The intercept and regression coefficients associated with this explanatory variable were fixed at 4.28 and 0.33, respectively, to mirror the parameters estimated in the real-world application (Section 5.1).

Two random effect structures were considered: the aggregated Gaussian process (AGP) and the Besag–York–Mollié (Besag et al., 1991, BYM), with model parameters corresponding to their fits to the real data. The AGP assumes a point-level GP aggregated at the areal unit level and is closer in structure to the HGP model. We chose AGP’s model parameters to reflect the HGP results from our real-world application (Section 5.1): a point-level marginal standard deviation ( $\sigma$ ) of 0.19, a smoothness parameter ( $\nu$ ) of 1, and a range parameter ( $\rho$ ) of 2.21. On the other hand, the BYM model represents a spatially correlated random effect closer to the structure of the DAGAR model. The BYM model was conveniently parametrized by the marginal precision (Riebler et al., 2016). We set the marginal stan-

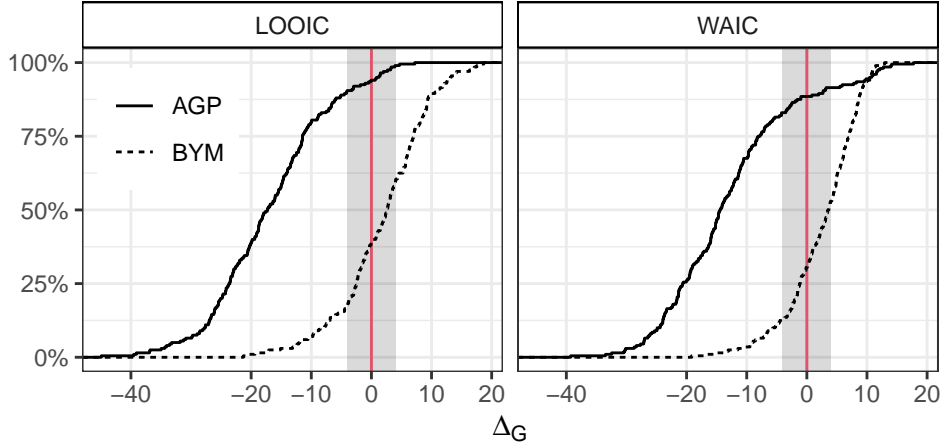


Figure 2: ECDFs displaying the GoF comparison between HGP and DAGAR models across different data generating processes (AGP: solid line, BYM: dashed line) and model comparison criteria (columns of the panel) based on 200 simulated datasets. Shaded region indicates negligible differences. Negative  $\Delta_G$  indicates better HGP performance.

dard deviation ( $\sigma$ ) to 0.24 and the spatial dependence parameter ( $\zeta$ ) to 0.43, aligning with estimates from the real data analyses in Section 5.1. Section D.1 of the appendix provides further details on the models used to generate data.

We generated 200 datasets from the Poisson GLMM under each of the two distinct random effect structures. For each simulated dataset, we fit two Bayesian Poisson GLMMs, the first one using an homoscedastic HGP while the second one using a DAGAR prior for the random effects. Both specified the fixed effects correctly with the single covariate. The priors for the parameters in the HGP model were set to be those presented in Section 3.2. The priors for the parameters in the DAGAR model were set to the same as those in (Datta et al., 2019). In particular, we set  $\pi(\beta_0) \propto 1$  and  $\beta_1 \sim N(0, 1000^2)$  for the regression parameters; a Gamma prior with shape 2 and rate 1 was placed on the conditional precision ( $\phi$ ), and a uniform prior between 0 and 1 on the spatial dependence parameter ( $\psi$ ). The GoF was evaluated using the criteria in Section 3.2, namely, LOOIC and WAIC, to compare which model fits the data better.

Figure 2 shows the HGP consistently fitting the data better than the DAGAR model when data were generated from the AGP. The figure displays empirical cumulative distribution

functions (ECDFs) of the differences ( $\Delta_G$ ) in LOOIC and WAIC (left and right columns of the panel, respectively) between the models. While no formal thresholds exist for significant differences in the model comparison criteria we used (Vranckx et al., 2021), we consider differences exceeding 4 noteworthy. For AGP-generated data (solid line), our simulation study provides strong evidence that the HGP outperforms the DAGAR in GoF. Specifically,  $\Delta_{\text{LOOIC}}$  was below  $-10$  for 80% of simulated datasets, strongly favoring the HGP. In contrast, evidence favoring DAGAR while exceeding ( $\Delta_{\text{LOOIC}} > 4$ ) was observed in only 1% of the generated data. Interestingly, the HGP remained competitive even when we generated data from the BYM model (a structure closer to the DAGAR). While there was some evidence favoring the DAGAR,  $\Delta_{\text{LOOIC}}$  was below 4 for more than 50% of the simulations under this scenario. These results highlight the HGP’s robustness as a disease mapping model, demonstrating superior performance when the data aligns with its structure and remains a viable option even when a specialized competitor better represents the underlying process.

In the appendix (Table A.4), we also evaluated the HGP’s ability to recover true model parameters under correct specification. We assessed estimation accuracy using Mean Absolute Percentage Error (MAPE) and the frequentist coverage percentage (CP) of 95% credible intervals. All model parameters achieved CPs close to the nominal level, with the lowest being 92.5% for  $\rho$ , which consistently proved the most challenging to estimate. The second most difficult parameter,  $\sigma$ , exhibited a maximum MAPE of only 7%.

## 4.2 Data Fusion

To assess the predictive performance of the HGP against standard data fusion models, we conducted a simulation study mirroring usual data fusion scenarios. Within a square region with an area of  $51^2$ , we generated a map comprising a  $17 \times 17$  grid-boxes of areal units (each with an area of  $3^2$ ) and 35 point-referenced data points. Additionally, we created five extra spatial units for each of the following three types of spatial units used exclusively to evaluate predictions: larger polygons (grid boxes with area of  $3^2$ ), smaller polygons (grid boxes with

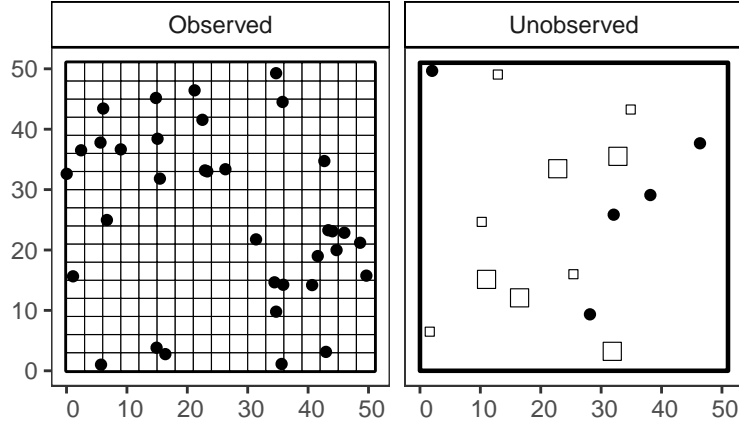


Figure 3: Maps utilized in the data fusion simulation study. The left map displays the region used for fitting the models, while the right map shows the data points used to evaluate the models’ predictive accuracy.

area of  $1.5^2$ ), and point-referenced, as displayed in Figure 3. We carefully chose the study region and grid box dimensions so each polygon’s area exceeded one, aligning with typical data fusion problems. This design emulates scenarios where areal units, often derived from satellite or computer models, are more abundant than point-referenced data. Hausdorff distances between sample units in this map ranged from 0.4 to 69.8. We simulate the datasets from a Normal GLMM with an identity link function, no covariates, and a spatial random effect. The overall mean of this GLMM was fixed at 6.28 to mirror the application from Section 5.2. In addition, this model introduces the small scale variance (denoted  $\tau^2$ ).

The two spatial random effects structures considered in the spatial GLMM are a heteroscedastic HGP and an AGP. For the HGP, the SD function  $v(\mathbf{s}) = \exp\{\alpha_0 + \alpha_1 \mathbb{1}(|\mathbf{s}| > 0)\}$  allows distinct variances for point-referenced and areal data. We selected HGP parameters ( $\tau^2 = 0.17^2$ ,  $\sigma = 4.4416$ ,  $\sigma_a = 1.3114$ ,  $\rho = 28.45$ , and  $\nu = 0.8$ ) to closely resemble the data analysis presented in Section 5.2. Note that the spatial variance for point and areal units ( $\sigma$  and  $\sigma_a$ , respectively) is a one-to-one transformation of  $(\alpha_0, \alpha_1)^\top$ . The dependence parameter,  $\rho$ , was adjusted to account for the scale of the map used in this simulation study.

The AGP model assumes:

$$Z(\mathbf{s}_i) = \begin{cases} \mathcal{A}(\mathbf{s}_i)^{-1} \int \mathbf{s}_i Z(\mathbf{s}) d\mathbf{s}, & \text{if } \mathcal{A}(\mathbf{s}_i) > 0, \\ Z(\mathbf{s}_i), & \text{otherwise,} \end{cases} \quad (9)$$

where  $\{Z(\mathbf{s}) : \mathbf{s} \in D\}$  is a zero-mean, second-order stationary GP with an isotropic Matérn covariance function with smoothness parameter  $\nu = 1$ . See [Moraga et al. \(2017\)](#) for a detailed definition of this function. We simulated AGP data with parameters  $\sigma^2 = 2.71^2$ ,  $\rho = 2.29$ , and  $\tau^2 = 1 \times 10^{-16}$ , again mirroring the real data analysis in [Section 5.2](#). In aggregated models,  $\tau$  approaches zero as only the average of homoscedastic independent residuals is observed, which converges in probability to zero.

We then generated 200 datasets from the Normal GLMM under each of the two different spatial random effects' structures detailed next. For each simulated dataset, we fit two Bayesian Normal GLMMs, one using the aforementioned heteroscedastic HGP prior for the random effect and the other using the AGP prior. When fitting the HGP model, we used the priors highlighted in [Section 3.2](#). In addition, we put a penalized complexity prior ([Simpson et al., 2017](#)) on  $\tau^{-2}$ , such that  $\mathbb{P}(\tau > a) = .05$ , where  $a$  is half the empirical SD observed in the data. Inferences and predictions were based in 2000 MCMC samples with a 1000 warm-up phase per chain with four parallel chains. The initialization of the algorithm is described in [Section 3.2](#).

Inferences for the model induced by the spatial random effect from [Equation \(9\)](#) were performed using the integrated nested Laplace approximation and the stochastic partial differential equation ([Lindgren et al., 2011](#), SPDE) method. The joint distribution induced by this AGP involve approximating stochastic integrals. Practitioners must define a grid with a fixed number of points within each areal unit to approximate these integrals ([Wang and Furrer, 2021](#)). The SPDE uses a mesh to discretize the space to achieve such an approximation efficiently. The number of grid points per polygon will depend on the resolution of the mesh. We used two different meshes to show the inferences and, consequently, the predictions

may change substantially depending on the accuracy of the approximation for the stochastic integrals in Equation (9). In the appendix , Figure A.9 visualizes these meshes: a sparse mesh (left column), and a fine-resolution mesh (second column), with approximately 2 and 25 points per polygon, respectively. Henceforth, we will differentiate the AGP models by mesh density, denoting the sparse-mesh model as AGP<sub>1</sub> and the fine-mesh model as AGP<sub>2</sub>. AGP model priors are detailed in Section E of the appendix .

We assess the quality of model predictions across different scenarios using four metrics. Firstly, point and interval predictions are derived from the posterior predictive distributions (Equation (8)), using their median and the 2.5% and 97.5% percentiles, respectively. The root mean square error of prediction (RMSP) is used to evaluate point estimates. The remaining three metrics assess interval predictions: the frequentist coverage percentage of prediction intervals, denoted CPP, their width, and the interval score (Gneiting and Raftery, 2007, IS). The latter is defined as

$$\text{IS}(y; l, u) = u - l + \frac{2}{\alpha}(l - y)\mathbb{1}\{y < l\} + \frac{2}{\alpha}(y - u)\mathbb{1}\{y > u\},$$

where  $l$  and  $u$  are the endpoints of the symmetric  $(1 - \alpha)\%$  prediction intervals for the target  $y$ .

Table 1 presents the prediction assessment metrics under both data-generating models at different types of spatial units. Let us first consider the “overall” case, that is, ignoring the types. When the AGP is the true model, the fine mesh AGP model yields the most accurate point predictions (lowest RMSP). However, the HGP model’s performance is only marginally worse, with a RMSP 18% higher. For interval predictions, the HGP model produces prediction intervals (PI) with near-nominal CPP and widths comparable to the AGP<sub>2</sub> model, resulting in a competitive interval score (IS). Despite having the narrowest PIs on average, the sparse-mesh AGP model suffers from poor coverage and, consequently, a high IS. As expected, when the true data-generating model is the HGP, the HGP model’s predic-

Table 1: Out-of-sample prediction for the three models under different data generating models. Spatial unit indicates the geometry of the sample units for which predictions were assessed; for polygons, area is additionally specified within parenthesis. Fit specifies the model fitted to the data. RMSP is the root mean squared error of prediction, CPP is the frequentist coverage percentage of the 95% prediction interval, Width is the prediction interval width, and IS is the interval score. Double headers denote the true data-generating model.

Spatial unit	Fit	AGP				HGP			
		RMSP	CPP	Width	IS	RMSP	CPP	Width	IS
Overall	AGP <sub>1</sub>	1.56	67.8	3.10	17.74	1.81	57.9	2.09	31.37
	AGP <sub>2</sub>	1.39	95.7	5.59	6.60	1.80	88.1	5.53	10.63
	HGP	1.65	90.8	6.10	8.65	1.51	95.7	6.15	7.05
Polygons (3 <sup>2</sup> )	AGP <sub>1</sub>	0.78	75.8	1.91	5.79	0.89	72.5	1.94	6.96
	AGP <sub>2</sub>	0.60	96.3	2.50	2.87	0.80	89.7	2.68	4.14
	HGP	0.83	97.9	3.78	4.00	0.74	96.4	3.00	3.36
Polygons (1.5 <sup>2</sup> )	AGP <sub>1</sub>	1.33	75.6	3.56	11.73	0.90	75.6	2.12	6.47
	AGP <sub>2</sub>	1.13	95.8	4.69	5.38	1.09	96.6	4.72	5.32
	HGP	1.50	79.2	3.84	9.36	0.85	94.8	3.36	4.01
Points	AGP <sub>1</sub>	2.56	52.2	3.85	35.70	3.64	22.8	2.20	80.70
	AGP <sub>2</sub>	2.43	95.1	9.59	11.54	3.51	77.9	9.19	22.42
	HGP	2.62	95.3	10.7	12.57	2.94	96.0	12.09	13.79

tive performance surpasses that of its competitors. The point predictions from both AGP models are remarkably similar, with the fine-mesh AGP exhibiting a RMSP only 19% higher than the correctly specified HGP. This suggests the fine-mesh AGP remains competitive in terms of point predictions, despite model misspecification. In terms of interval predictions, while the AGP<sub>2</sub> was competitive, its sparse mesh counterpart delivered poor interval predictions. The performance of the competing method varies considerably depending on the mesh resolution, which can significantly impact prediction accuracy. In contrast, our model eliminates the need for arbitrary mesh selection and consistently delivers highly competitive predictions, enhancing prediction accuracy.

Table 1 further reveals demonstrates a consistent decline in prediction accuracy for all models as the area of the spatial units decreased. For AGP-generated data, the AGP<sub>2</sub> model’s RMSP for point-referenced data was approximately four times higher than for the

polygons with bigger area (i.e.,  $3^2$ ). Similarly, the HGP model’s RMSP increased by a factor of 3.15 for the same comparison (point-referenced vs largest polygon). For both the HGP and AGP<sub>2</sub>, CPP remained near the nominal level for all the spatial units. However, HGP’s CPP dropped below nominal level for smaller polygons (area of  $1.5^2$ ). This is likely due to variance underestimation: while the AGP-generated data’s variance is inversely proportional to spatial units, the fitted HGP model only distinguish between points and polygons, not their area. Regarding the IS, both our model and the AGP<sub>2</sub> model showed IS values roughly three times higher for point-referenced data compared to the largest polygons. This aligns with the simulation parameters. The AGP<sub>1</sub> model’s IS performance deteriorated substantially when decreasing the area of the spatial units.

Under the HGP data-generating process, the HGP model consistently outperformed competitors on all assessment metrics except PI width. Although point predictions were broadly similar across models, the HGP provided remarkably superior interval predictions for all spatial unit types, maintaining CPP near the nominal level (see Table 1. In contrast, the AGP<sub>1</sub> model exhibited a CPP of only 22.8% for point-referenced data. The poor coverage for both AGP models with point-referenced data is further reflected in their IS, which were 5.9 (AGP<sub>1</sub>) and 1.6 (AGP<sub>2</sub>) times higher than the HGP. On the other hand, the AGP<sub>2</sub> model remained competitive with the HGP for polygons interval predictions, while the sparse AGP performed poorly.

Table A.6 in the appendix presents the results for parameter estimation under the correct specification of the the HGP model. We used the same metrics as in Section 4.1 to assess the parameters estimation. The MAPE for  $\rho$  was around 10.9% while for  $\sigma_a$  it was 9.21%. Similarly to what is observed with geostatistical models, the small scale standard deviation parameter, namely  $\tau$ , was the most challenging parameter to be estimated. Unlike the areal simulation, the coverage of some of the variance parameters was consistently below the nominal level of 95%. This results are expected, as the HGP inherits the weak identifiability of these parameters from geostatistical models under a normal likelihood (Zhang, 2004).

Predictions remain trustworthy despite this issue.

## 5 Applications

### 5.1 Areal Data: Respiratory Disease Hospitalization

We first analyze a dataset on the count of hospital admissions due to respiratory disease in 2010 for the 134 intermediate zones (IZ) to the north of the river Clyde in the Great Glasgow and Clyde health board in Scotland. This dataset is publicly available in the `CARBayesdata` package (Lee, 2022). For each IZ, the expected number of admissions based on the national age- and sex-standardized rates, alongside the percentage of people classified as income deprived in each IZ are also available. The standardized morbidity ratio (SMR), the ratio between the number of observed and expected cases, is often used to control for confounding factors when estimating risks (Greenland, 1984). The goals of the analyses are: (1) to provide smooth estimates of the SMR, adjusted for the percentage of income deprivation, and (2) to contrast the outcomes from the proposed methodology with other established methods.

In this application,  $Y(\mathbf{s}_i)$  is the number of admissions by respiratory disease registered at the  $i$ -th IZ, denoted  $\mathbf{s}_i$ . In the  $i$ -th IZ, define  $x_i$  as the percentage of people who are defined to be income deprived and  $E_i$  as the expected number of admissions. We analyze the data using the GLMM model from Section 3.1, with a Poisson likelihood, a log link function, an intercept, a covariate  $x_i$ , and an offset  $E_i$ . We employed the homoscedastic HGP (with a PEC function with smoothness  $\nu = 0.7$ ) as the prior for the random effects; the choice of  $\nu = 0.7$  is justified in Table A.7 of the appendix. The priors for the parameters in the HGP GLMM were set to be those presented in Section 3.2. Inference was performed using four parallel chains with 5000 MCMC samples, thinned by 10, after discarding the initial 1000 iterations as the warm-up period. The initialization of the algorithm is described in Section 3.2. The highest split- $\hat{R}$  was smaller than 1.01, providing evidence of convergence.

Two competing models, BYM and DAGAR, were considered as the priors for the spatial

Table 2: Parameter estimates and model comparison criteria for the three models fitted to the areal dataset. Marginal posterior summary through median and 95% credible intervals.

	HGP	DAGAR	BYM
$\beta_0$	-0.21 (-0.268, -0.139)	-0.26 (-0.450, -0.137)	-0.22 (-0.254, -0.184)
$\beta_1$	0.33 (0.284, 0.368)	0.31 (0.258, 0.370)	0.33 (0.285, 0.366)
$\sigma$	0.19 (0.155, 0.234)	0.30 (0.218, 0.484)	0.24 (0.176, 0.354)
$\rho$	2.25 (0.159, 6.948)		
$\psi$		0.43 (0.069, 0.827)	
$\xi$			0.42 (0.100, 0.815)
LOOIC	<b>1081.0</b>	1081.9	1089.3
WAIC	1038.0	<b>1032.4</b>	1039.6

random effects  $\mathbf{z}$  for comparison, as outlined in Sections 4.1 and D.1, respectively. In the BYM model, parametrized by the marginal precision (Riebler et al., 2016), we followed Morris et al. (2019) and set standard normal priors for the intercept ( $\beta_0$ ), regression coefficient ( $\beta_1$ ), and the logit of the mixing parameter  $\zeta$ . Similarly, a standard normal distribution truncated on positive real numbers was used for  $\sigma$ . The priors for the DAGAR model are the ones presented in Section 4.1. The initialization of the MCMC algorithm followed the same principle used for the HGP model. In both cases, we used four parallel chains with a warm-up period of 4000 iterations and based the inferences on 20000 MCMC samples, thinned by 20. For these models, the parameters split- $\hat{R}$  provided evidence of convergence. In addition, trace and density plots for posterior samples of all fitted model parameters are provided in Section F.1 of the appendix.

We present the posterior medians and 95% CIs for the parameters from the HGP, DAGAR, and BYM models in Table 2. When considering the coefficient linked to the covariate representing income deprivation, all three models yield similar posterior estimates. The positive posterior estimates the respective parameter ( $\beta_1$ ) indicate a positive association between proportion of income deprived people and hospitalization rates for respiratory diseases. Among these models, DAGAR exhibits the broadest credible intervals for the intercept, whereas the marginal posterior distribution for this parameter in the BYM model is

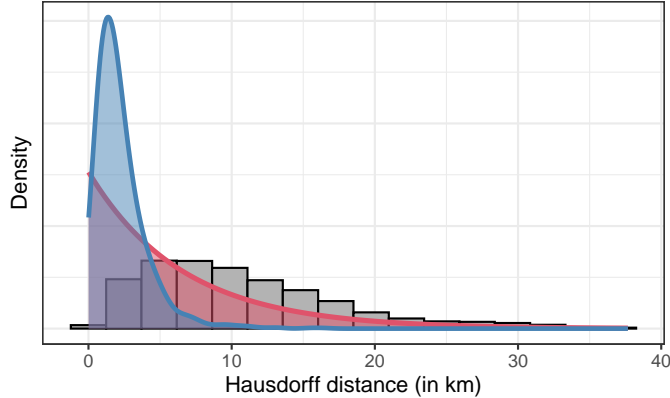


Figure 4: Density histogram of the pairwise Hausdorff distances observed in the dataset and. In blue, estimated posterior density of the practical range  $\rho$ , and, in red, the prior used for  $\rho$ .

highly concentrated around  $-0.22$ . Examining the spatial aspect, the confidence interval for the practical range parameter  $\rho$  in the HGP model implies that the distance at which the spatial correlation between random effects from two distinct spatial units decreases to 0.10 is at most 6.95 kilometers. Conversely, the 95% CI for the spatial dependence parameter  $\psi$  from the DAGAR model spans from 0.07 to 0.83. In other words, this credible interval suggests that the clustering effect ranges from almost negligible to very strong. A similar pattern is observed for the  $\zeta$  in the BYM model.

To gain a better understanding of this value in the context of the data, Figure 4 displays a density histogram of all pairwise Hausdorff distances observed in the dataset. The plot also features the prior distribution (in red) and estimated posterior density (in blue) associated with the practical range. Notably, the majority of the posterior distribution mass for  $\rho$  falls below the concentration of most pairwise distances, indicating a negligible clustering effect in hospital admissions. An additional analysis of the spatial correlation is presented in Section F in the appendix .

In Table 2, we also present two model comparison criteria described in Section 4 for the models fitted to the data. These results suggest the HGP stands out as the best fit based on the LOOIC, rendering the HGP prior a competitive fit for these data. Despite the modest improvement in model fitting capacity, the HGP possesses an advantage in terms of intuitive

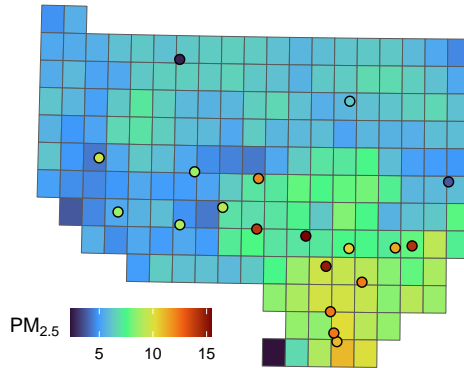


Figure 5:  $\text{PM}_{2.5}$  in Ventura and Los Angeles counties in California, United States. Points represent direct measurements. Tiles are satellite derived estimates.

interpretability of its spatial dependence, achieved in the last two paragraphs through the practical range parameter  $\rho$ . Among the specialized models for areal data, the BYM was the least adequate in this application. However, none of the models delivered a remarkably better fit to this dataset. This is further reinforced by looking at the maps of observed and smoothed SMR estimates presented in Figure A.10 from the appendix.

## 5.2 Data fusion: Air pollution in Ventura and Los Angeles

Our second application analyzes fused fine particulate matter ( $\text{PM}_{2.5}$ ) data in Ventura and Los Angeles counties, California, USA. The dataset combines point-referenced direct measurements (EPA, 2018) from 1999 to present with areal satellite-derived estimates (Van Donkelaar et al., 2015), averaged from 2010 to 2012 (Figure 5). To align temporally, we averaged the direct measurements over the same period. The study region comprises 19 measurement stations and 184 grid boxes (approximately  $101.95 \text{ km}^2$  each), excluding islands. Our primary goal is to predict  $\text{PM}_{2.5}$  concentrations at a finer scale (approximately  $45 \text{ km}^2$ ) using both data sources. Secondly, we aim to estimate average  $\text{PM}_{2.5}$  concentration and its spatial dependence across both counties.

Building on previous concepts, we introduce the notation for this application. The re-

sponse variable is the recorded  $\text{PM}_{2.5}$ , noted  $Y(\mathbf{s}_i)$  at the spatial unit  $\mathbf{s}_i$ , which is either a point or a grid box. We again resort to the GLMM model from Section 3.1. In this case, there are no covariates, the likelihood is Normal with variance  $\tau^2$ , and the link function is the identity. A heteroscedastic HGP prior is placed on the random effect allowing for differing variances between point-referenced and areal data through the SD function from Equation (2) with  $w(\mathbf{s}) = \mathbb{1}(\mathcal{A}(\mathbf{s}) > 0)$ . For interpretability, we present results for  $\sigma = \exp\{\alpha_0\}$  and  $\sigma_a = \exp\{\alpha_0 + \alpha_1\}$  instead of  $\alpha_0$  and  $\alpha_1$ . The model was fit with  $\nu$  fixed at different values, and we selected the model with best goodness-of-fit ( $\nu = 0.8$ ). For more details, see Table A.8 in the appendix. The priors for model parameters are as in Section 4.2. The MCMC algorithm initialization is described in Section 3.2. We used four parallel chains, each comprising a warm-up period of 2000 samples and an additional 2000 samples for inference. All model parameters exhibited split- $\hat{R}$  values below, indicating good convergence. This is further supported by the trace plots presented in Section G.1 of the appendix.

For comparison, we also fit an AGP random effect model, with priors for the model parameters as described in Section 4.2. Two meshes of different resolutions were considered; see Figure A.24 in the appendix. The sparse- and fine-mesh AGP models are denoted  $\text{AGP}_1$  and  $\text{AGP}_2$ , respectively.

We present the posterior median and 95% CI of the model parameters in Table 3. When looking at the common parameters between the three models (namely,  $\beta_0$ ,  $\sigma$ ,  $\rho$ , and  $\tau$ ), the HGP acts as a compromise between  $\text{AGP}_1$  and  $\text{AGP}_2$  while eliminating the arbitrary choice of the level of discretization for approximating numerical integrals. Unlike the aggregated models, our method allows the data to tell us whether the variance of the underlying spatial parameter is smaller or larger than the same quantity for point-referenced data. Interestingly, the estimated SD of the point-referenced data is 3.09 times larger than the areal data (95% CI: 2.43, 4.12). The interpretation of  $\rho$ , presented in tens of kilometers, in both models is carried out in a similar fashion because the Hausdorff distance between points is equivalent to the distance between points used by the AGP models.

Table 3: Parameter estimates and out-of-sample prediction assessment for the three models fitted to the fused dataset. Marginal posterior summary through median and 95% credible intervals. RMSP is the root mean squared error of prediction; CPP is the frequentist coverage of the 95% prediction interval; Width is the width of the prediction interval; and IS is the interval score.

	HGP	AGP <sub>1</sub>	AGP <sub>2</sub>
$\beta$	5.605 (4.688, 6.449)	6.219 (2.16, 10.10)	6.187 (5.879, 6.478)
$\rho$	13.826 (7.817, 23.608)	13.163 (5.140, 30.244)	0.632 (0.456, 0.832)
$\tau$	0.178 (0.073, 0.312)	1.394 (1.242, 1.563)	0.539 (0.394, 0.719)
$\sigma$	3.849 (2.921, 5.181)	1.703 (0.960, 2.910)	2.399 (2.024, 2.837)
$\sigma_a$	1.241 (1.037, 1.505)		
RMSP	<b>1.05</b>	1.45	1.64
Width	3.57	<b>2.53</b>	9.67
CPP	95.5	78.6	95.5
IS	<b>4.80</b>	15.11	13.65

Table 3 also presents the out-of-sample prediction performance of the three models, assessed via 10-fold cross-validation. Using four metrics from our prior simulation study (RMSP, CPP, prediction interval width, IS), we find the HGP offers the most reliable point predictions, evidenced by its lowest RMSP. The HGP also maintains nominal coverage for its prediction intervals. While the AGP<sub>2</sub> achieves similar coverage, its prediction intervals are considerably wider, resulting in inferior interval scores. Further analysis by data type is detailed in Table A.9 of the appendix, revealing the unreliability of competing methods for point-referenced data, where frequentist coverage can be as low as 3%.

The drastic differences in the AGP results for different mesh resolutions are striking. The credible interval width for the intercept varies significantly between the two models. Crucially, the practical range reveals a key divergence: AGP<sub>1</sub> indicates moderate spatial dependence, while AGP<sub>2</sub> suggests weak dependence, likely explaining the observed overfitting in the latter. This weak dependence may imply AGP<sub>2</sub> assigns nearly independent random intercepts to each data point, with variances inversely proportional to the sample unit’s area. AGP mesh resolution is typically practitioner-informed, and results are highly sensitive to this tuning parameter, which lacks a consensus on “optimal resolution” (Fuentes and Raftery,

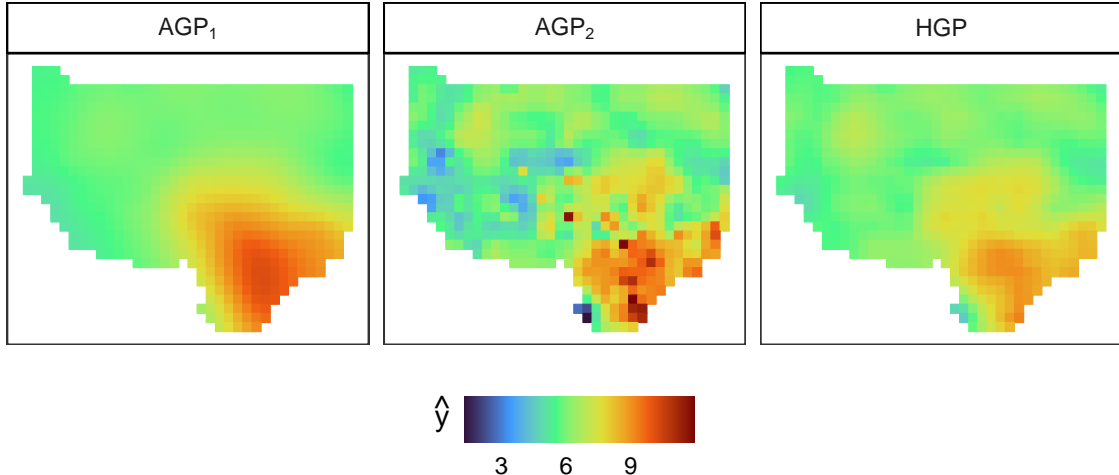


Figure 6: Change-of-support of  $\text{PM}_{2.5}$  to a finer resolution using the sparse and fine AGP and the HGP priors.

2005; Liu et al., 2011; Wang and Furrer, 2021).

Figure 6 displays the change-of-support predictions provided by the three models we fitted to the data. HGP predictions indicate higher  $\text{PM}_{2.5}$  concentrations in the southeast (Los Angeles) and provide precise estimates with uncertainty quantification in areas lacking measurement stations, such as the northwestern part of the map. Unlike its counterparts, the HGP’s ability to generate parsimonious predictions without arbitrary discretization, combined with its interpretable parameters, makes it an attractive alternative for spatial data fusion problems.

## 6 Discussion

The proposed framework unifies the modeling of spatial data, extending geostatistical models to include areal and fused data within the same setting. We established conditions under which the PEC function of the HGP is positive definite, ensuring its validity. As a prior for spatial random effects in a GLMM, the HGP proves to be competitive to specialized models for diverse spatial data types. Our simulation studies indicate that the HGP is particularly advantageous for areal data with units of varying sizes and shapes, as confirmed by our

disease mapping application. Unlike its specialized counterparts, the HGP also provides a directly interpretable spatial parameter, offering insights into the practical range of spatial dependence. In data fusion contexts, the HGP delivers more reliable interval predictions compared to the sparse AGP, and it provided similar results to the fine AGP in parameter estimation and spatial range. Additionally, in the air pollution data application, the proposed model consistently outperformed the AGP regardless of the resolution of its mesh. This success is even more remarkable considering the HGP bypasses the subjective step of defining a grid or mesh, a crucial but problematic requirement for the AGP. In addition, independent of the spatial data type, it continues to have direct and interpretable parameters.

Our proposed methodology shares the “big  $n$ ” computational complexity challenge inherent in traditional geostatistical approaches. Consequently, the computational cost of evaluating the finite-dimensional likelihood induced by the HGP for a set of  $n$  areal units scales as  $\mathcal{O}(n^3)$ . Proving the validity of the PEC function under the Hausdorff distance on Euclidean space was a demanding theoretical task. Relaxing the isotropy assumption for this function presents further theoretical complexities. Moreover, to apply the HGP to data measured on manifolds (like the sphere), new theoretical results are needed to guarantee the positive definiteness of a correlation function within that specific geometric context.

The HGP framework offers numerous opportunities for development. Further researching its theoretical properties will strengthen the foundation for its applications. A crucial focus should be developing correlation functions designed specifically for the HGP, particularly those suited to scenarios where spatial data is observed on a sphere. Approximations inspired by methods like the Nearest Neighbor Gaussian Process (Datta et al., 2016; Quiroz et al., 2023) or reduced rank approximations (Solin and Särkkä, 2020) could significantly broaden the applicability of the HGP to large-scale datasets. These advancements hold the potential to establish the HGP as an even more powerful and versatile tool for spatial data analysis.

## References

- Assunção, R. and Krainski, E. (2009), “Neighborhood Dependence in Bayesian Spatial Models,” *Biometrical Journal: Journal of Mathematical Methods in Biosciences*, 51, 851–869.
- Backurs, A. and Sidiropoulos, A. (2016), “Constant-distortion Embeddings of Hausdorff Metrics into Constant-dimensional  $l_p$  Spaces,” in *Approximation, Randomization, and Combinatorial Optimization. Algorithms and Techniques (APPROX/RANDOM 2016)*, eds. Jansen, K., Mathieu, C., Rolim, J. D. P., and Umans, C., Dagstuhl, Germany: Schloss Dagstuhl – Leibniz-Zentrum für Informatik, vol. 60 of *Leibniz International Proceedings in Informatics (LIPIcs)*, pp. 1:1–1:15.
- Bakar, K. S. and Jin, H. (2020), “Areal Prediction of Survey Data Using Bayesian Spatial Generalised Linear Models,” *Communications in Statistics - Simulation and Computation*, 49, 2963–2978.
- Banerjee, A., Dunson, D. B., and Tokdar, S. T. (2012), “Efficient Gaussian Process Regression for Large Datasets,” *Biometrika*, 100, 75–89.
- Banerjee, S. and Gelfand, A. E. (2002), “Prediction, Interpolation and Regression for Spatially Misaligned Data,” *Sankhyā: The Indian Journal of Statistics, Series A*, 64, 227–245.
- Besag, J. (1974), “Spatial Interaction and the Statistical Analysis Of Lattice Systems,” *Journal of the Royal Statistical Society. Series B (Methodological)*, 36, 192–236.
- Besag, J., York, J., and Mollié, A. (1991), “Bayesian Image Restoration, with Two Applications in Spatial Statistics,” *Annals of the Institute of Statistical Mathematics*, 43, 1–20.
- Cressie, N. (1993), *Statistics for Spatial Data*, Wiley Series in Probability and Statistics, Nashville, TN: John Wiley & Sons.

- Cruz-Reyes, D. L., Assunção, R. M., and Loschi, R. H. (2023), “Inducing High Spatial Correlation with Randomly Edge-Weighted Neighborhood Graphs,” *Bayesian Analysis*, 18, 1247 – 1281.
- Curriero, F. C. (2006), “On the Use of Non-Euclidean Distance Measures in Geostatistics,” *Mathematical Geology*, 38, 907–926.
- Datta, A., Banerjee, S., Finley, A. O., and Gelfand, A. E. (2016), “Hierarchical Nearest-neighbor Gaussian Process Models For Large Geostatistical Datasets,” *Journal of the American Statistical Association*, 111, 800–812.
- Datta, A., Banerjee, S., Hodges, J. S., and Gao, L. (2019), “Spatial Disease Mapping Using Directed Acyclic Graph Auto-regressive (DAGAR) Models,” *Bayesian analysis*, 14, 1221 – 1244.
- Diggle, P. J., Tawn, J. A., and Moyeed, R. A. (1998), “Model-based Geostatistics,” *Journal of the Royal Statistical Society Series C: Applied Statistics*, 47, 299–350.
- EPA, U. (2018), “Clean Air Status and Trends Network (CASTNET),” <https://www.epa.gov/outdoor-air-quality-data/download-daily-data>, accessed: September 22, 2022.
- Fuentes, M. and Raftery, A. E. (2005), “Model Evaluation and Spatial Interpolation by Bayesian Combination of Observations with Outputs from Numerical Models,” *Biometrics*, 61, 36–45.
- Gelfand, A. E., Kim, H.-J., Sirmans, C., and Banerjee, S. (2003), “Spatial Modeling with Spatially Varying Coefficient Processes,” *Journal of the American Statistical Association*, 98, 387–396.
- Gelfand, A. E., Zhu, L., and Carlin, B. P. (2001), “On the Change of Support Problem for Spatio-temporal Data,” *Biostatistics*, 2, 31–45.

- Gelman, A. (2006), “Prior Distributions for Variance Parameters in Hierarchical Models (Comment on Article by Browne and Draper),” *Bayesian Analysis*, 1, 515–534.
- Gneiting, T. and Raftery, A. E. (2007), “Strictly Proper Scoring Rules, Prediction, and Estimation,” *Journal of the American statistical Association*, 102, 359–378.
- Gonçalves, F. B. and Gamerman, D. (2018), “Exact Bayesian Inference in Spatiotemporal Cox Processes Driven by Multivariate Gaussian Processes,” *Journal of the Royal Statistical Society: Series B (Statistical Methodology)*, 80, 157–175.
- Gotway, C. A. and Young, L. J. (2002), “Combining Incompatible Spatial Data,” *Journal of the American Statistical Association*, 97, 632–648.
- Greenland, S. (1984), “Bias in Methods for Deriving Standardized Morbidity Ratio and Attributable Fraction Estimates,” *Statistics in Medicine*, 3, 131–141.
- Hoffman, M. D. and Gelman, A. (2014), “The No-U-turn Sampler: Adaptively Setting Path Lengths in Hamiltonian Monte Carlo,” *Journal of Machine Learning Research*, 15, 1593–1623.
- Lee, D. (2022), *CARBayesdata: Data Used in the Vignettes Accompanying the CARBayes and CARBayesST Packages*, r package version 3.0.
- Li, D., Tang, W., and Banerjee, S. (2023), “Inference for Gaussian Processes with Matérn Covariogram on Compact Riemannian Manifolds,” *Journal of Machine Learning Research*, 24, 1–26.
- Lindgren, F. and Rue, H. (2015), “Bayesian Spatial Modelling with R-INLA,” *Journal of Statistical Software*, 63, 1–25.
- Lindgren, F., Rue, H., and Lindström, J. (2011), “An Explicit Link Between Gaussian Fields and Gaussian Markov Random Fields: The Stochastic Partial Differential Equation

- Approach,” *Journal of the Royal Statistical Society: Series B (Statistical Methodology)*, 73, 423–498.
- Liu, Z., Le, N. D., and Zidek, J. V. (2011), “An Empirical Assessment of Bayesian Melding for Mapping Ozone Pollution,” *Environmetrics*, 22, 340–353.
- McElreath, R. (2016), *Statistical Rethinking: A Bayesian Course with Examples in R and Stan*, New York, NY: Chapman and Hall/CRC.
- Moraga, P., Cramb, S. M., Mengersen, K. L., and Pagano, M. (2017), “A Geostatistical Model for Combined Analysis of Point-level and Area-level Data Using INLA and SPDE,” *Spatial Statistics*, 21, 27–41.
- Morris, M., Wheeler-Martin, K., Simpson, D., Mooney, S. J., Gelman, A., and DiMaggio, C. (2019), “Bayesian Hierarchical Spatial Models: Implementing the Besag York Mollié Model in Stan,” *Spatial and Spatio-temporal Epidemiology*, 31, 100301.
- Palacios, M. B. and Steel, M. F. J. (2006), “Non-Gaussian Bayesian Geostatistical Modeling,” *Journal of the American Statistical Association*, 101, 604–618.
- Quiroz, Z. C., Prates, M. O., Dey, D. K., and Rue, H. (2023), “Fast Bayesian Inference of Block Nearest Neighbor Gaussian Models for Large Data,” *Statistics and Computing*, 33, 54.
- Richards, D. S. P. (1985), “Positive Definite Symmetric Functions on Finite-dimensional Spaces II,” *Statistics & Probability Letters*, 3, 325–329.
- Riebler, A., Sørbye, S. H., Simpson, D., and Rue, H. (2016), “An Intuitive Bayesian Spatial Model for Disease Mapping That Accounts for Scaling,” *Statistical Methods in Medical Research*, 25, 1145–1165.
- Rodrigues, E. C. and Assunção, R. (2012), “Bayesian Spatial Models with a Mixture Neighborhood Structure,” *Journal of Multivariate Analysis*, 109, 88–102.

- Sendov, B. (2004), “Hausdorff Distance and Image Processing,” *Russian Mathematical Surveys*, 59, 319–328.
- Shephard, G. and Webster, R. (1965), “Metrics for Sets of Convex Bodies,” *Mathematika*, 12, 73–88.
- Simpson, D., Rue, H., Riebler, A., Martins, T. G., and Sørbye, S. H. (2017), “Penalising Model Component Complexity: A Principled, Practical Approach to Constructing Priors,” *Statistical science*, 32, 1–28.
- Solin, A. and Särkkä, S. (2020), “Hilbert Space Methods for Reduced-rank Gaussian Process Regression,” *Statistics and Computing*, 30, 419–446.
- Team, S. D. (2023), “RStan: the R interface to Stan,” R package version 2.32.3.
- Van Donkelaar, A., Martin, R. V., Brauer, M., and Boys, B. L. (2015), “Global Annual PM2.5 Grids from MODIS, MISR and SeaWiFS Aerosol Optical Depth (AOD), 1998–2012,” Accessed on Aug 15, 2022.
- Vehtari, A., Gelman, A., and Gabry, J. (2017), “Practical Bayesian Model Evaluation Using Leave-one-out Cross-validation and WAIC,” *Statistics and computing*, 27, 1413–1432.
- Vehtari, A., Gelman, A., Simpson, D., Carpenter, B., and Bürkner, P.-C. (2021), “Rank-normalization, Folding, and Localization: An Improved  $\hat{R}$  for Assessing Convergence of MCMC (with discussion),” *Bayesian Analysis*, 16, 667–718.
- Vranckx, M., Neyens, T., and Faes, C. (2021), “The (in)Stability of Bayesian Model Selection Criteria in Disease Mapping,” *Spatial Statistics*, 43, 100502.
- Wang, C. and Furrer, R. (2021), “Combining Heterogeneous Spatial Datasets with Process-based Spatial Fusion Models: A Unifying Framework,” *Computational Statistics & Data Analysis*, 161, 107240.

Watanabe, S. (2010), “Asymptotic Equivalence of Bayes Cross Validation and Widely Applicable Information Criterion in Singular Learning Theory,” *Journal of Machine Learning Research*, 11, 3571–3594.

Zhang, H. (2004), “Inconsistent Estimation and Asymptotically Equal Interpolations in Model-based Geostatistics,” *Journal of the American Statistical Association*, 99, 250–261.

## A Proof of Proposition 2.1

Theorem 11 in [Backurs and Sidiropoulos \(2016\)](#) guarantees the existence of a probabilistic embedding of  $h^\nu$ , for  $\nu \in (1/2, 1)$ , into high- and constant-dimensional  $L_1$  normed Euclidean space. Let  $\mathbf{x} \in \mathbb{R}^d$ , with  $d \geq 3$ , and  $\|\cdot\|_1^\nu$  be the  $L_1$  norm raised to the power  $\nu$ . Then, Proposition 3.1 in [Richards \(1985\)](#) establishes that  $\|\mathbf{x}\|_1^\nu$  is conditionally negative definite for  $\nu \in (0, 1]$ . Finally,  $\exp\{-ad(\cdot)\}$  is positive definite for any  $a > 0$  if and only if  $d(\cdot)$  is conditionally negative definite ([Curriero, 2006](#), and references therein). Combining these results we establish the positive definiteness property of the PEC function for the specified range of  $\nu$ .

## B Empirical assessment of positive definiteness of PEC function

Building on our theoretical analysis, we empirically assess the positive definiteness of the PEC function for  $\nu \in (0, 1]$ . We first calculate Hausdorff distance matrices for the areal and fused data, defined in Sections 5.1 and 5.2, respectively. Evaluating the PEC function across these matrices with  $\nu \in [0.01, 1]$  and  $\rho \in [d_{\min}, d_{\max}]$  (where  $d_{\min}$  and  $d_{\max}$  are the dataset’s minimum and maximum distances) yields corresponding correlation matrices. We then compute each matrix’s smallest eigenvalue. A negative eigenvalue suggests the corresponding PEC function is not positive definite. However, even valid covariance functions can

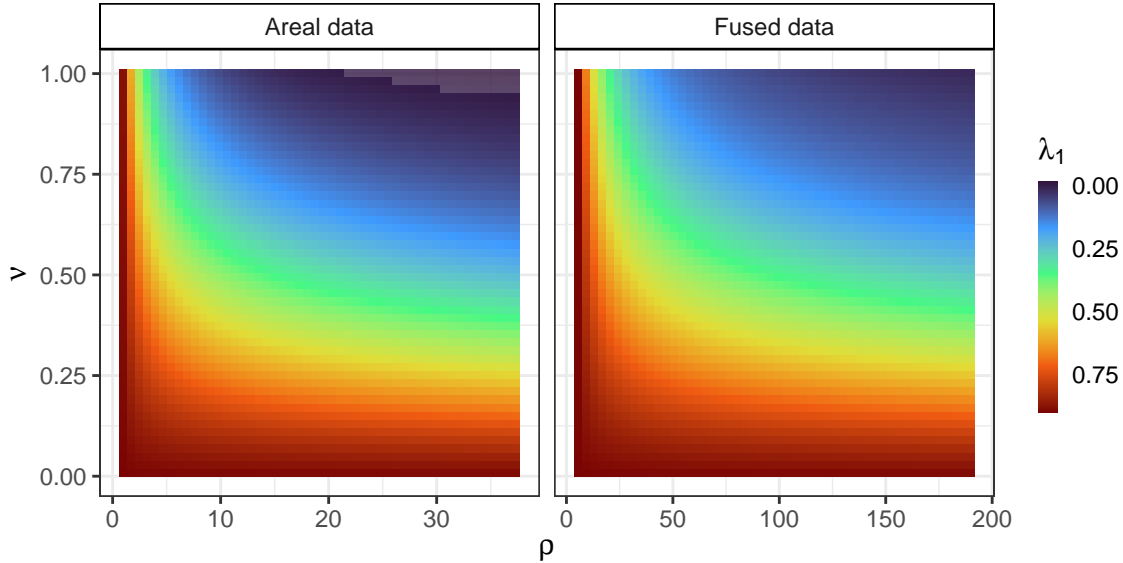


Figure A.7: Smallest eigenvalue of the powered exponential correlation matrix under different combinations of smoothness ( $\nu$ ) and practical range ( $\rho$ ) for areal and fused data. The transparency indicates regions where  $\lambda_1 < 0$ .

be ill-conditioned or nearly rank-deficient at dense locations or when there exists a severely strong spatial dependence (Banerjee et al., 2012).

Figure A.7 displays the smallest eigenvalues ( $\lambda_1$ ) of the PEC-induced correlation matrices for both datasets. The fused data exhibits positive eigenvalues for all  $(\nu, \rho)$  pairs. Conversely, the areal data reveals some small negative eigenvalues (range  $-0.0099$  to  $-0.00006$ ) under severely strong spatial dependence and at  $\nu \approx 1$ , the border of the parametric space. Therefore, our empirical study confirms our theoretical result on the positive definiteness of the PEC function and provides evidence it may be possible to extend it to  $\nu \in (0, 1]$ .

## C Sampling from the posterior predictive distribution of the HGP

Efficient sampling from Equation (8) utilizes the MCMC samples obtained during parameter estimation (Section 3.2). For each MCMC sample  $b$ , we generate a corresponding Monte Carlo sample from the posterior predictive distribution of  $\mathbf{Y}^*$ . First, using GP proper-



Figure A.8: Study region encompassing the northern portion of Greater Glasgow, Scotland, delimited by the River Clyde. Coordinates are referenced to the OSGB36 datum and projected in the British National Grid.

ties (Diggle et al., 1998), we sample from:

$$(\mathbf{Z}_{(b)}^* \mid \mathbf{Z} = \mathbf{z}(b)) \sim \mathcal{N}(\mu_{\mathbf{s}^*|\mathbf{s}}, \Sigma_{\mathbf{s}^*|\mathbf{s}}),$$

where  $\mathbf{z}_{(b)}$  is the  $b$ -th MCMC sample of the spatial random effect, and  $\mu_{\mathbf{s}^*|\mathbf{s}}$  and  $\Sigma_{\mathbf{s}^*|\mathbf{s}}$  are the conditional mean and covariance matrix induced by the HGP (Equation (1)). Next, we sample  $\mathbf{y}_{(b)}^*$  from  $p(\mathbf{y}^* \mid \boldsymbol{\theta}_{(b)}, \mathbf{z}_{(b)}^*)$ , where  $\boldsymbol{\theta}_{(b)}$  is the  $b$ -th MCMC sample of  $\boldsymbol{\theta}$ . This yields a Monte Carlo sample of the predictive posterior distribution of  $\mathbf{Y}^*$ , allowing estimation of various quantities associated with the distribution.

## D Complementary results for Section 4.1

### D.1 Details on AGP and BYM

Figure A.8 displays the map where we generate data in the areal simulation study.

**AGP** Specifically, the AGP assumes  $Z(\mathbf{s}_i) = \mathcal{A}(\mathbf{s}_i)^{-1} \int_{\mathbf{s}_i} K(\mathbf{s})d\mathbf{s}$ , where  $\{K(\mathbf{s}) : \mathbf{s} \in D\}$  is a (point-level) zero-mean, second order stationary and isotropic GP (Cressie, 1993, p. 53) defined over the study region. Provided we have set a correlation function and its parameters, we simulate data from this model as follows: We first generate a fine grid of points over the study region. At each point, we generate data from a GP. Next, the realizations of the spatial random effect at the areal sample units are obtained by averaging the data simulated at the grid points within each areal unit.

**BYM** The BYM model corresponds to a zero-mean random effect with covariance matrix given by  $\sigma^{-2}((1-\zeta)\mathbf{I}+\zeta\mathbf{Q}^-)$ , where  $\sigma$  is the marginal SD,  $\mathbf{I}$  is the identity matrix, and  $\mathbf{Q}^-$  is the generalized inverse of the scaled precision matrix of an ICAR model (Riebler et al., 2016). The spatial dependence parameter  $\zeta$  is a mixing parameter. Its parametric space comprises of real numbers between 0 and 1, with larger values indicate stronger spatial dependence.

## D.2 Additional simulation results

In Table A.4, we present the bias of estimation, root mean square error (RMSE), and frequentist coverage percentage of the credible intervals for the parameters in the HGP along with the parameters used to generate the datasets in the areal data simulation study. Although  $\rho$  is a harder parameter to estimate, our model has delivered credible intervals with good coverage for this parameter.

## E Complementary results for Section 4.2

Figure A.9 displays two resolutions of meshes for each simulation scenario in the data fusion setting.

The priors for the parameters and hyperparameters of the data fusion AGP model are taken from Moraga et al. (2017). That is, for  $\beta_0$  we set a flat improper prior and a log-Gamma (shape 1 and rate  $5 \times 10^{-5}$ ) for the log of the precision of the measurement error

Table A.4: Assessing parameter estimation for HGP model for areal data. Scenario indicates the data configuration scenario, True is the parameter used to simulate the datasets, Bias is the bias of estimation, MAPE is the mean absolute percentage error, RMSE is the root mean square error of estimation, and CP is the frequentist coverage percentage of the credible interval.

Scenario	Parameter	True	Bias	MAPE	RMSE	CP
$15 \times 15$ grid	$\beta_1$	4.290	0.002	1.3	0.115	95.5
	$\beta_2$	0.330	0.004	8.9	0.058	95.0
	$\rho$	1.654	0.439	45.6	1.536	95.0
	$\sigma$	0.436	0.014	7.0	0.058	93.5
$15 \times 15$ grid	$\beta_1$	4.290	-0.005	1.0	0.089	95.5
	$\beta_2$	0.330	0.002	6.4	0.044	95.5
	$\rho$	1.971	0.398	31.1	1.318	95.0
	$\sigma$	0.436	0.009	5.0	0.043	95.5
Map	$\beta_1$	4.390	0.001	1.2	0.104	95.5
	$\beta_2$	0.330	0.001	10.9	0.063	92.5
	$\rho$	2.320	0.812	56.3	2.735	92.5
	$\sigma$	0.436	0.012	7.4	0.061	95.0

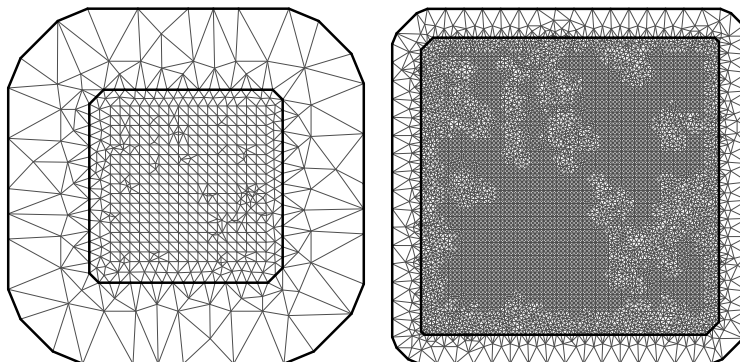


Figure A.9: This panel presents sparse and fine meshes on its top and bottom rows, respectively. The first column of the panel corresponds to the map for the simulation scenario 1, while the second column is associated to simulation scenario 2.

variance (i.e.,  $\log(\tau^2)$ ). Lastly, for  $[\sigma^2, \rho]^\top$ , the authors use multivariate normal prior on a non-linear transformation of these two parameters (Lindgren and Rue, 2015).

Table A.5 displays the same results as in Table 1 from the main paper but for a different sample size. The polygons used to simulate data here are in a  $15 \times 15$  grid. Everything else is the same as in Section 4.2. The results follow the same trend as observed in the main text. That is, in general, the HGP does a good job quantifying uncertainty and seems to be

Table A.5: Out-of-sample prediction for the three models under different data generating models. DGM stands for the data generation model, MAPE is the mean absolute percentage error of prediction; RMSP is the root mean square error of prediction; IS is the interval score, and CPP is the frequentist coverage of the 95% prediction interval.

DGM	Fit	MAPE	RMSP	IS	CPP
AGP	HGP	8.35	1.84	9.41	90.4
	AGP <sub>1</sub>	8.26	1.73	16.23	74.4
	AGP <sub>2</sub>	<b>7.33</b>	<b>1.57</b>	<b>7.03</b>	92.2
HGP	HGP	<b>17.36</b>	<b>1.78</b>	<b>7.47</b>	96.1
	AGP <sub>1</sub>	27.09	2.26	31.94	60.6
	AGP <sub>2</sub>	30.34	2.29	10.90	87.9

Table A.6: Assessing parameter estimation for HGP model for fused data. Map indicates the size of the grid where the data was simulated, True is the parameter used to simulate the datasets, Bias is the bias of estimation, MAPE is the mean absolute percentage error, RMSE is the root mean square error of estimation, and CP is the frequentist coverage percentage of the credible interval.

Map	Parameter	True	Bias	MAPE	RMSE	CP
15 × 15 grid	$\beta_1$	5.810	0.014	5.568	0.402	91.5
	$\rho$	20.366	-0.967	12.351	3.221	99.0
	$\sigma_a$	1.311	-0.154	12.183	0.192	81.5
	$\sigma$	4.442	-0.125	11.784	0.634	91.5
	$\tau$	0.170	0.252	148.432	0.265	66.5
17 × 17 grid	$\beta_1$	5.810	-0.022	4.903	0.358	90.0
	$\rho$	27.934	0.003	10.927	3.836	99.5
	$\sigma_a$	1.311	-0.115	9.121	0.145	84.5
	$\sigma$	4.442	-0.150	8.616	0.477	93.5
	$\tau$	0.170	0.170	99.788	0.181	79.5

more trustworthy under model misspecification.

In Table A.6, we present the bias of estimation, root mean square error (RMSE), and frequentist coverage percentage of the credible intervals for the parameters in the HGP along with the parameters used to generate the datasets in the fused data simulation study. We present the parameter estimation results for two sizes of simulated maps. Similarly to what we encounter in the geostatistics literature,  $\tau$  is hard to estimate. However, as we increased the sample size, the estimation of this parameter has improved considerably. In addition, despite the low bias, when estimating the practical range parameter ( $\rho$ ), the coverage of the

Table A.7: Different model comparison criteria for the homoscedastic HGP models fit with different values for  $\nu$ .

	$\nu = 0.6$	$\nu = 0.7$	$\nu = 0.8$	$\nu = 0.9$
LOOIC	1091.9	<b>1081.5</b>	1092.6	1090.8
WAIC	1039.3	<b>1038.7</b>	1039.3	1039.2
DIC	1049.5	<b>1048.8</b>	1049.4	1049.6

credible intervals and the RMSE indicate high uncertainty around the estimation of such parameter.

## F Complementary results for Section 5.1

To choose the most appropriate value of  $\nu$  in our application, we have fitted out model with  $\nu \in \{0.6, 0.7, 0.8, 0.9\}$ . These values were selected because they fill different regions of the parameter space where the PEC function is positive definite. The goodness-of-fit metrics associated to each value of  $\nu$  are presented in Table A.7.

In Figure A.10, we display the observed SMR along with its smoothed estimates provided by the three different models we fit to this data. The smoothed estimates look nearly identical, further suggesting the three models deliver very similar goodness-of-fit for these data.

Figure A.11 shows the spatial correlations induced by the DAGAR and HGP in the random effects as functions of the Hausdorff distance. Once again, it is noticeable that the HGP has less uncertainty around its estimates of spatial correlations. In addition, the upper bound of the spatial correlation function of the HGP touches the mean curve of the DAGAR, while the lower bounds of the two distributions of curves are very close to each other.

### F.1 Convergence check for areal application

Figures A.12 and A.13 display the trace and density plots for the HGP model parameters. In addition, Figures A.14 and A.15 present the same analysis for some of the sampled random

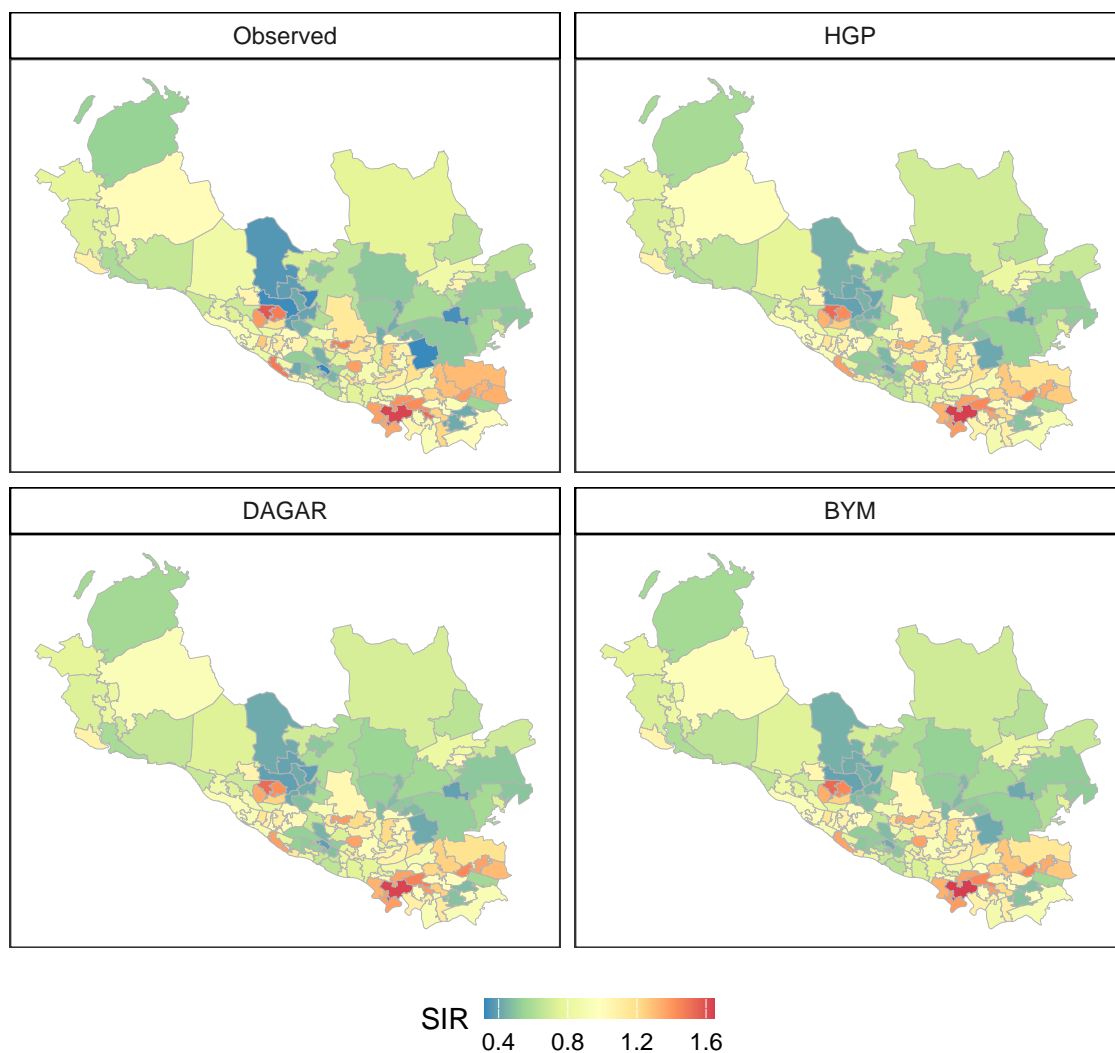


Figure A.10: Panel presenting the observed SMR and its estimated values from the HGP, DAGAR, and BYM, respectively.

effects.

Figures A.16 and A.17 display the trace and density plots for the BYM model parameters. In addition, Figures A.18 and A.19 present the same analysis for some of the sampled random effects.

Figures A.20 and A.21 display the trace and density plots for the DAGAR model parameters. In addition, Figures A.22 and A.23 present the same analysis for some of the sampled random effects.

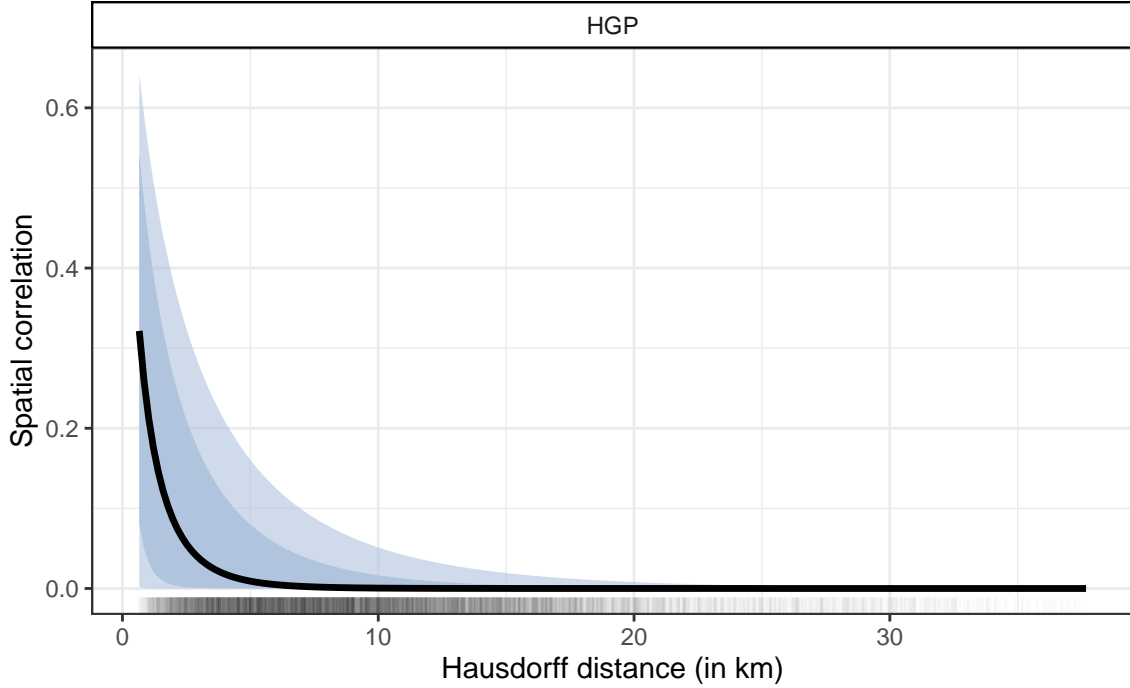


Figure A.11: Spatial correlation between random effects as a function of the Hausdorff distance.

Table A.8: Different model comparison criteria for the heteroscedastic HGP models fit with different values for  $\nu$ .

	$\nu = 0.6$	$\nu = 0.7$	$\nu = 0.8$	$\nu = 0.9$
LOOIC	511.0	506.2	<b>505.1</b>	511.5
WAIC	516.4	507.9	<b>507.2</b>	512.1
DIC	480.0	471.7	<b>468.7</b>	469.7

## G Complementary results for Section 5.2

Figure A.24 presents the different meshes used by the AGP models in the data fusion application.

The most appropriate value of  $\nu$  in our application was chosen based on the goodness-of-fit when fitting our model with  $\nu \in \{0.6, 0.7, 0.8, 0.9\}$ . These values were selected because they fill different regions of the parameter space where the PEC function is positive definite. The goodness-of-fit metrics associated to each value of  $\nu$  are presented in Table A.8.

Table A.9 presents the predictive performance of the HGP and aggregated models using

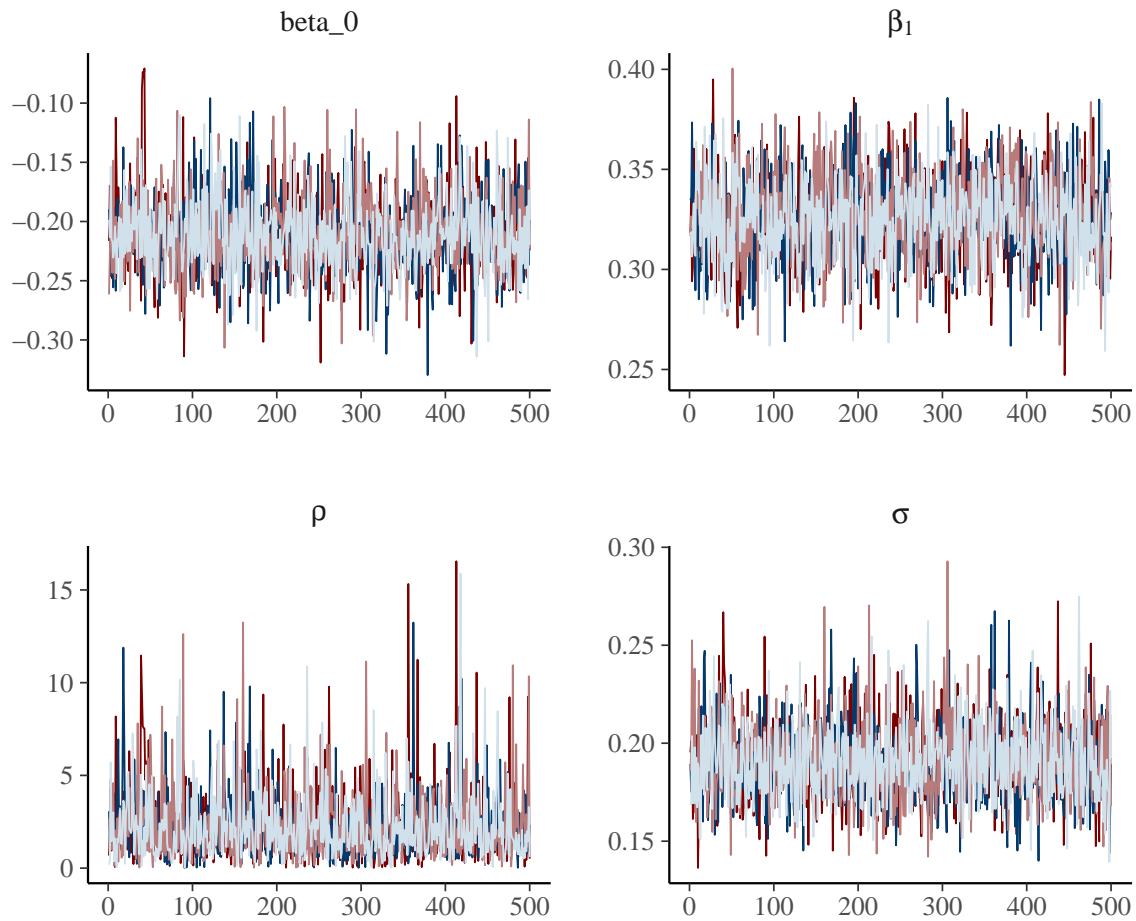


Figure A.12: Traceplots of the parameters associated to the HGP model fitted to the areal data.

a 10-fold cross-validation. It summarizes how each model performed specifically for the point referenced and areal (polygon) data. In terms of point prediction, HGP has shown a better performance regardless of the geometry type. The same behavior was observed for interval predictions. The AGP models tend to be overconfident in their interval predictions for point-referenced data, resulting in very low coverage.

## G.1 Convergence check for data fusion application

Figures A.25 and A.26 display the trace and density plots for the HGP model parameters.

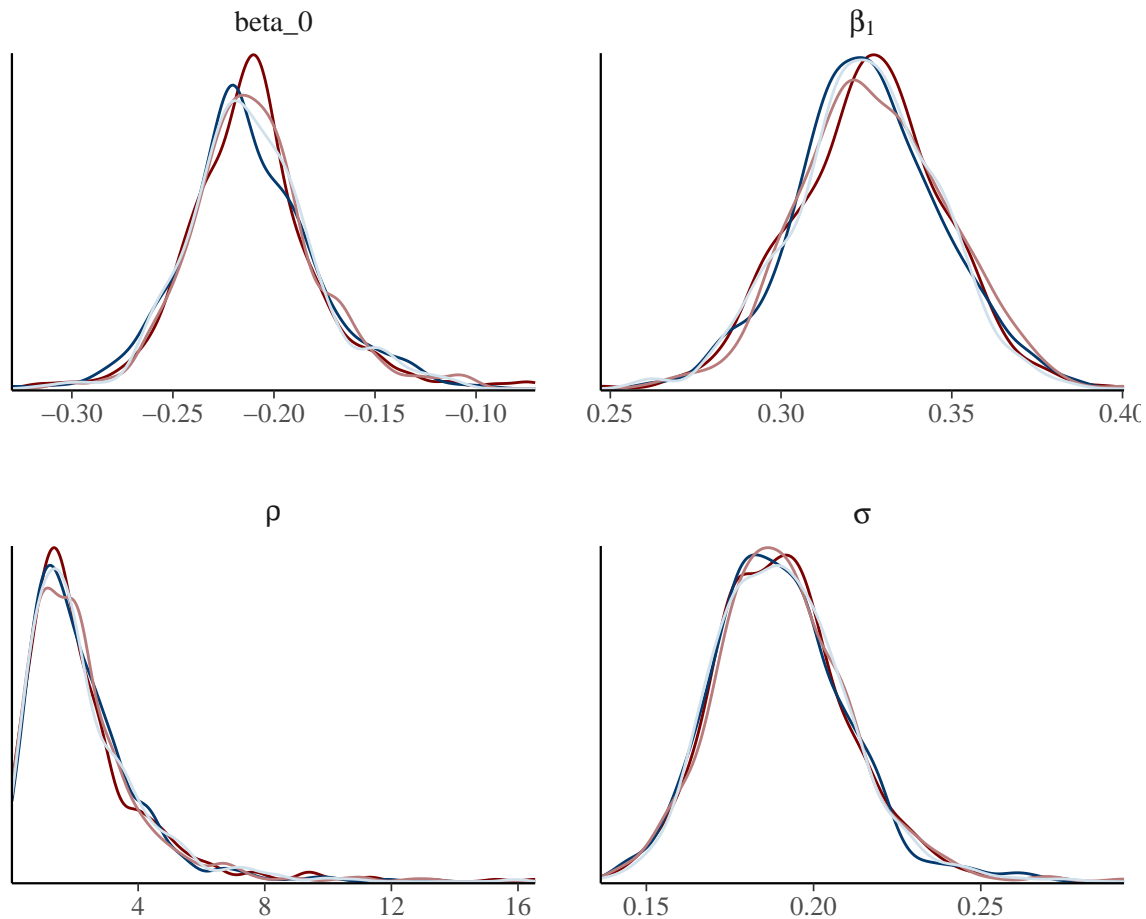


Figure A.13: Estimated densities of the parameters associated to the HGP model fitted to the areal data.

Table A.9: Metrics for assessment of out-of-sample predictions using 10-fold cross-validation for different geometry resolutions. RMSP is the root mean squared error of prediction; CPP is the frequentist coverage of the 95% prediction interval; Width is the width of the prediction interval; and IS is the interval score.

Resolution	Model	RMSP	CPP	Width	IS
Point	HGP	2.71	85.4	9.6	12.69
	AGP <sub>1</sub>	4.07	3.12	2.4	111.84
	AGP <sub>2</sub>	2.71	57.3	8.2	45.03
Polygon	HGP	0.62	96.9	2.9	3.83
	AGP <sub>1</sub>	0.86	86.6	2.5	6.03
	AGP <sub>2</sub>	1.10	98.9	9.8	10.92

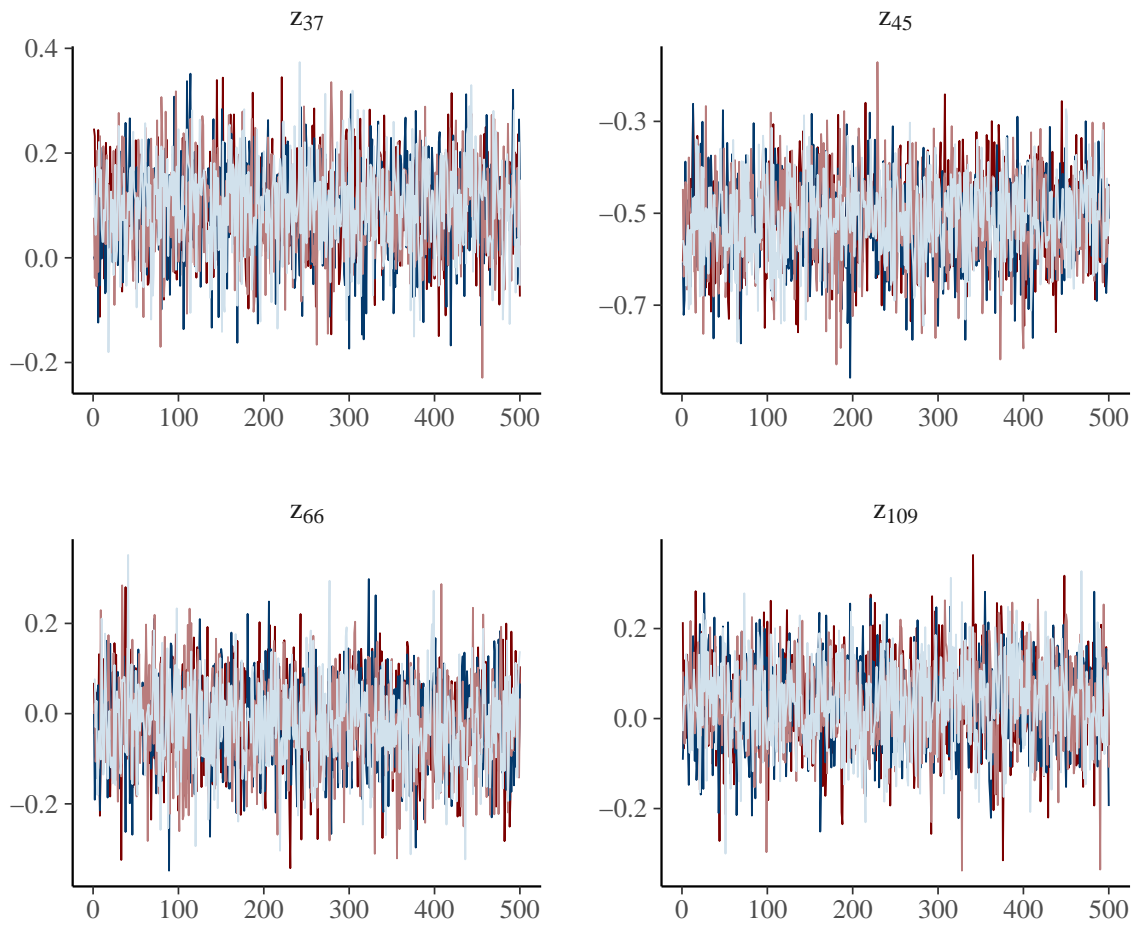


Figure A.14: Traceplots of randomly chosen random effects from the HGP model fitted to the areal data.

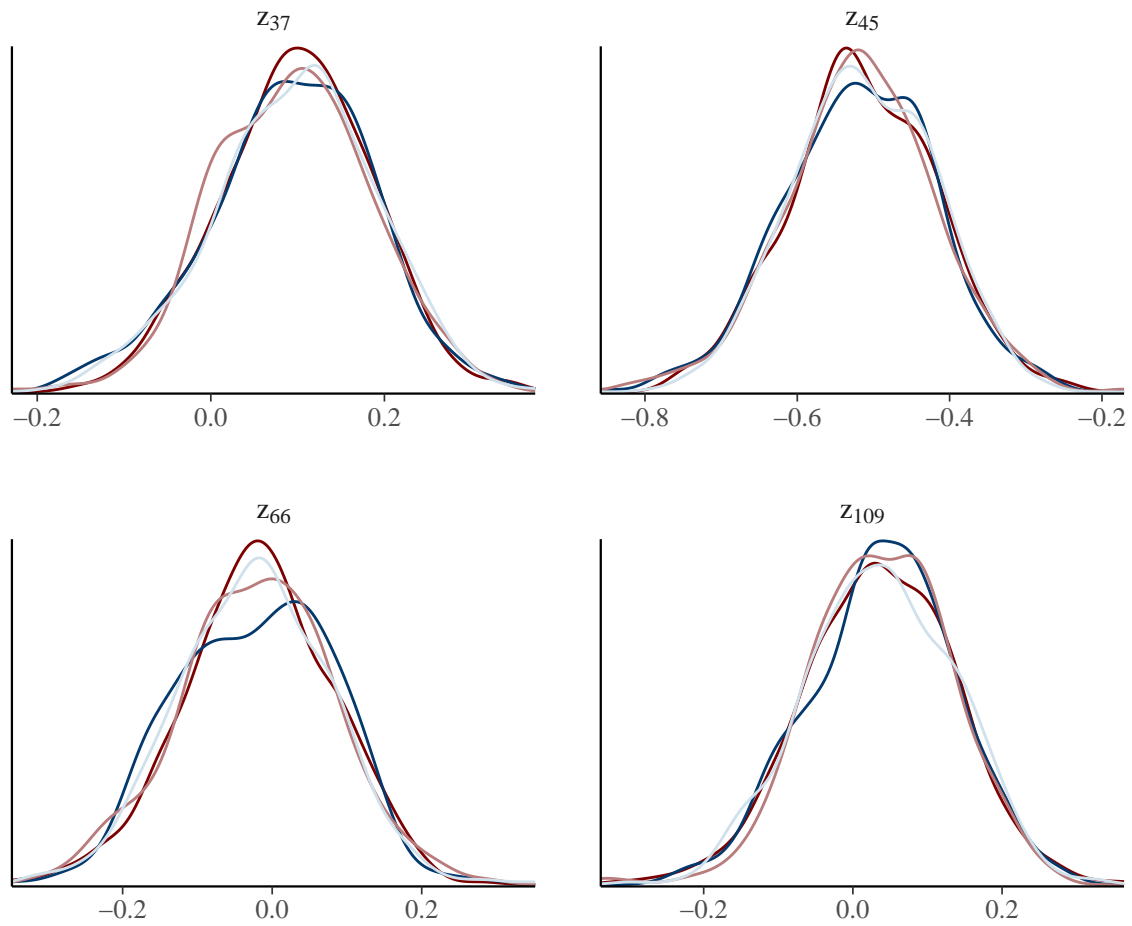


Figure A.15: Estimated densities of randomly chosen random effects from the HGP model fitted to the areal data.

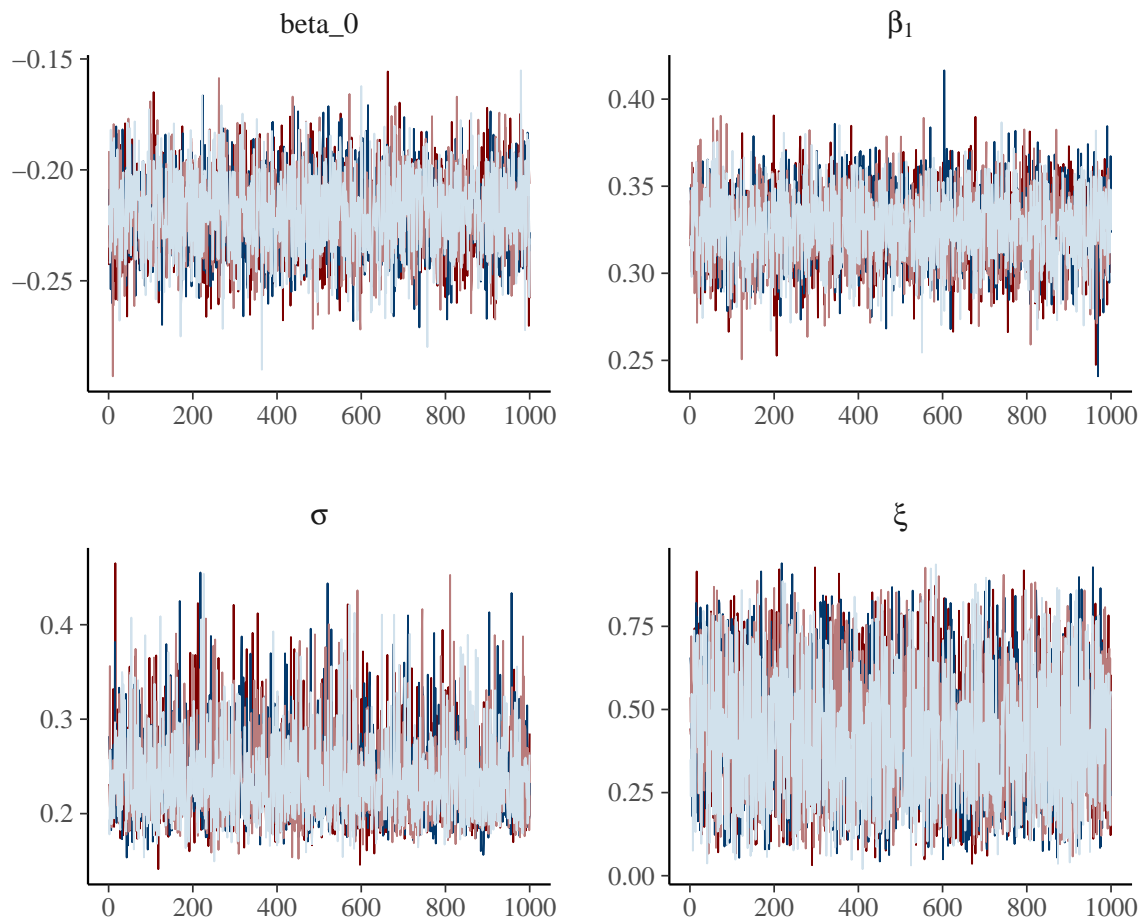


Figure A.16: Traceplots of the parameters associated to the BYM model fitted to the areal data.

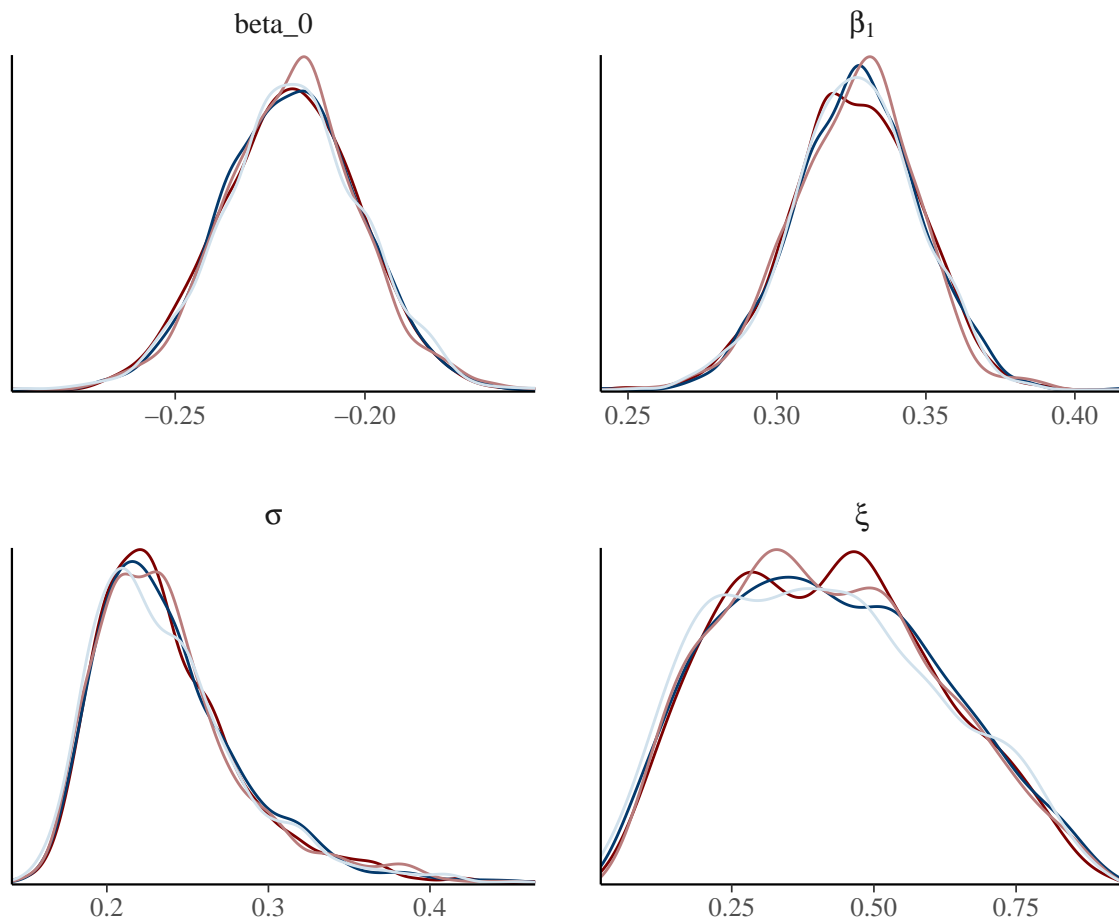


Figure A.17: Estimated densities of the parameters associated to the BYM model fitted to the areal data.

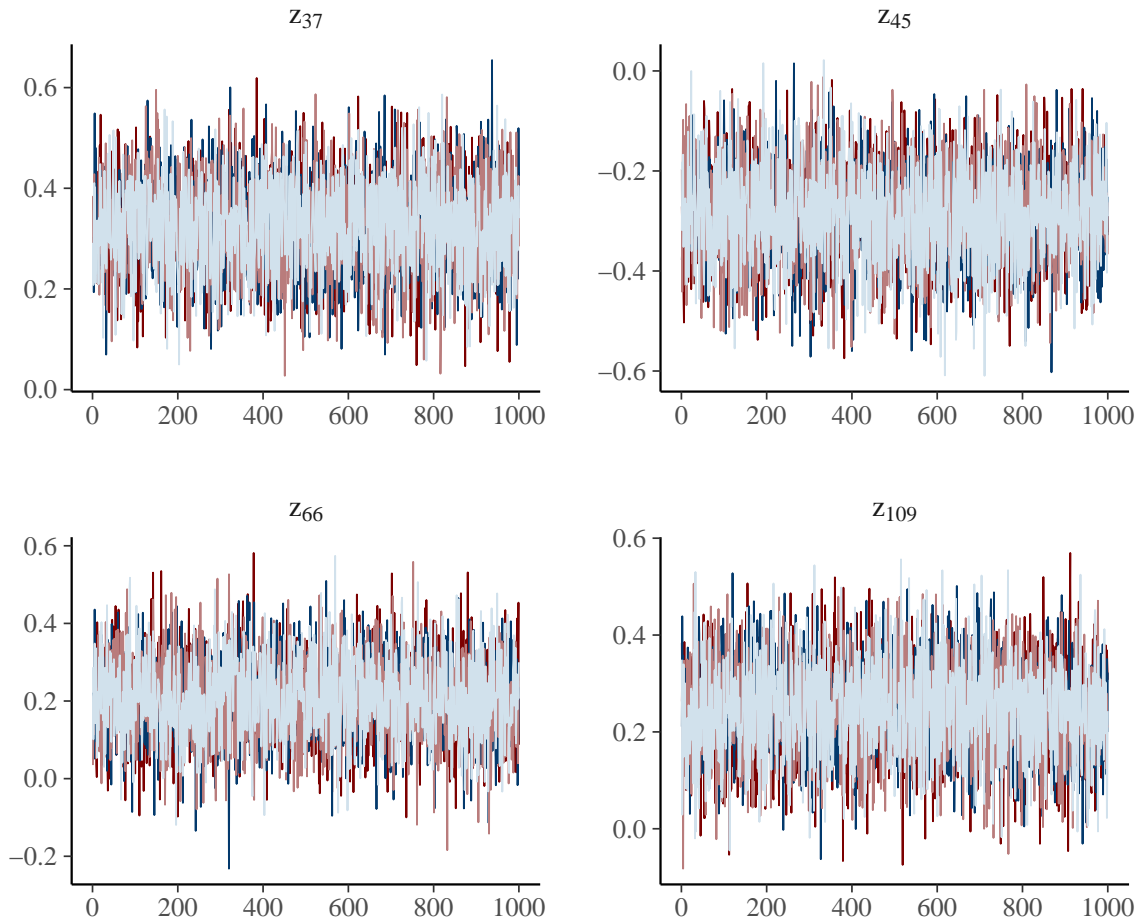


Figure A.18: Traceplots of randomly chosen random effects from the BYM model fitted to the areal data.

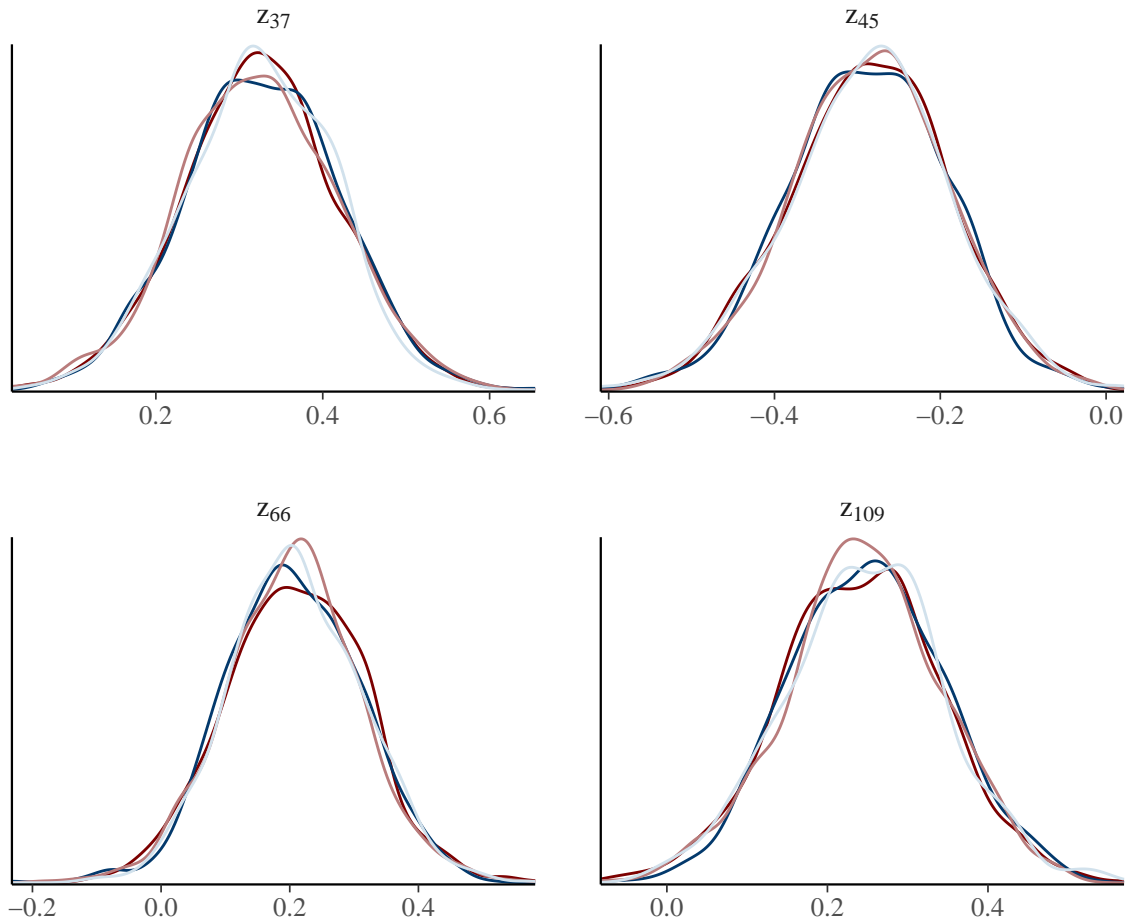


Figure A.19: Estimated densities of randomly chosen random effects from the BYM model fitted to the areal data.

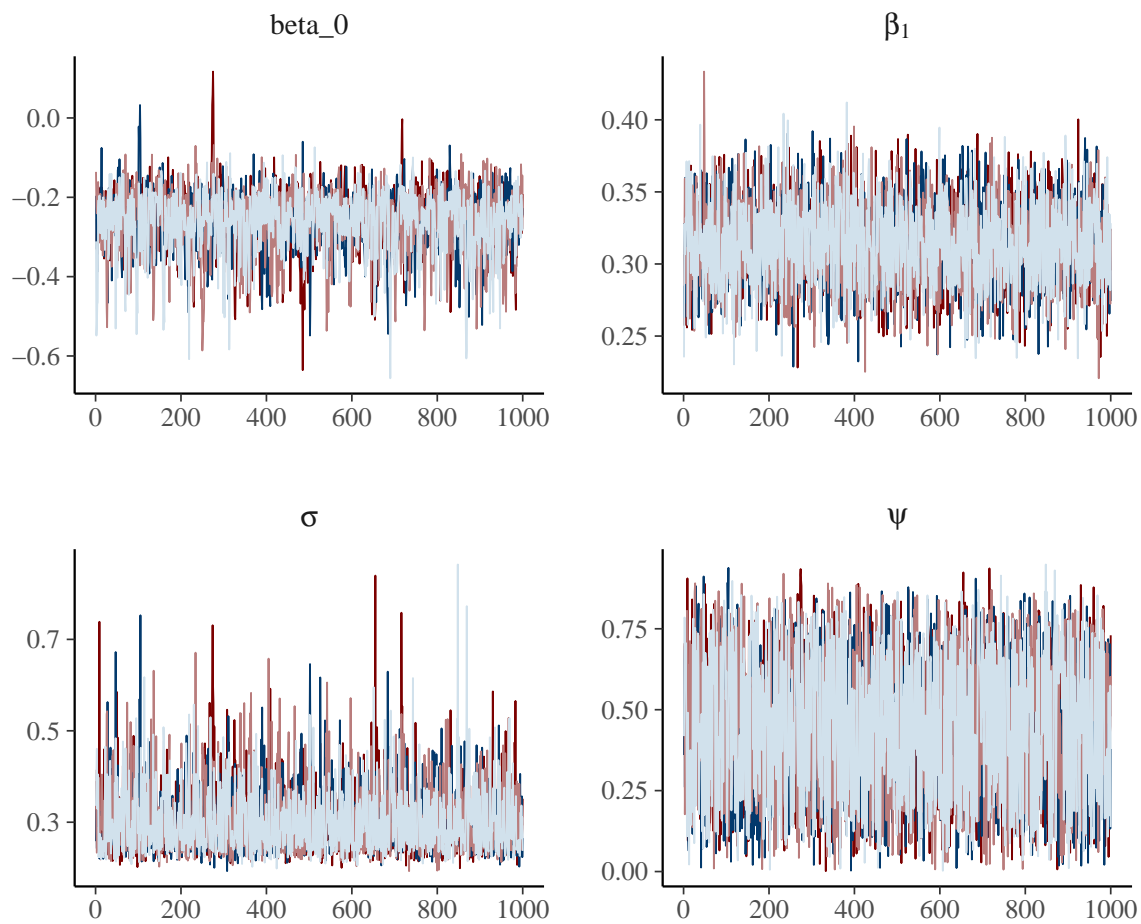


Figure A.20: Traceplots of the parameters associated to the DAGAR model fitted to the areal data.

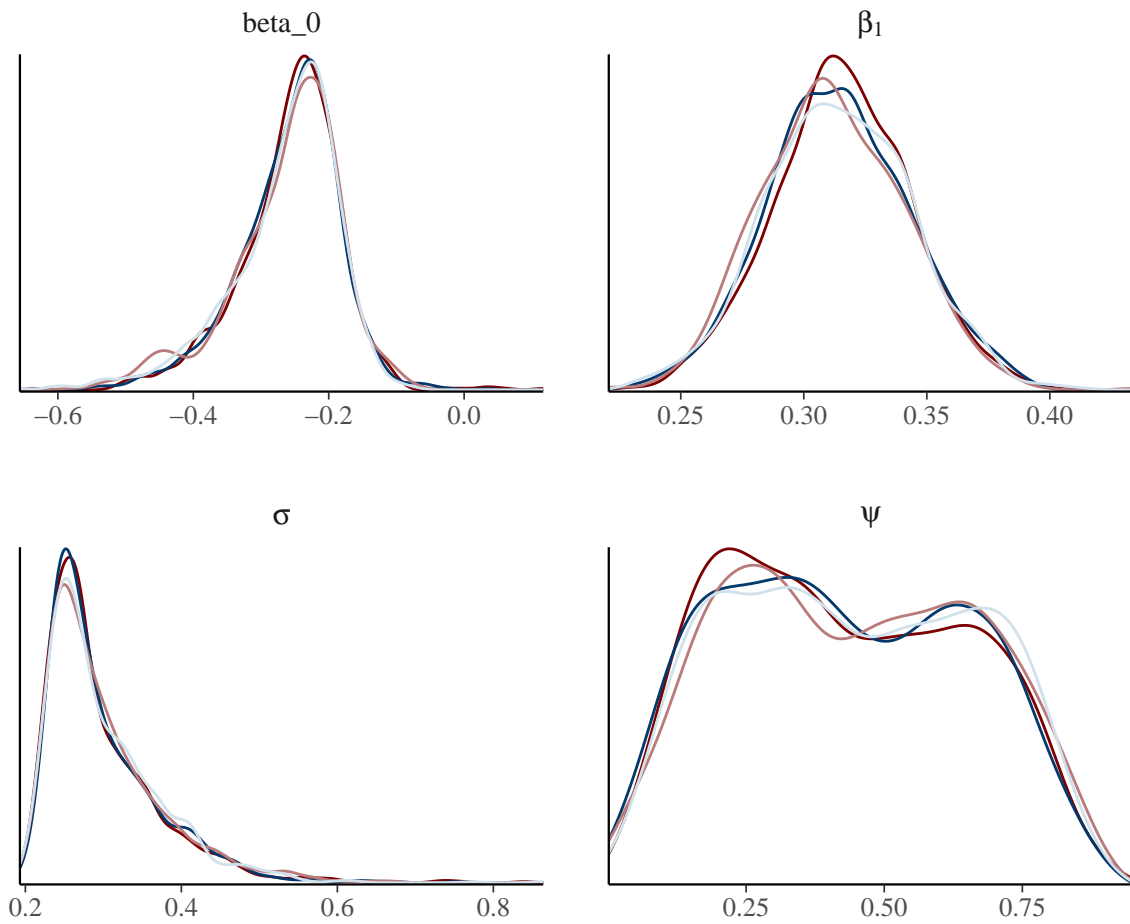


Figure A.21: Estimated densities of the parameters associated to the DAGAR model fitted to the areal data.

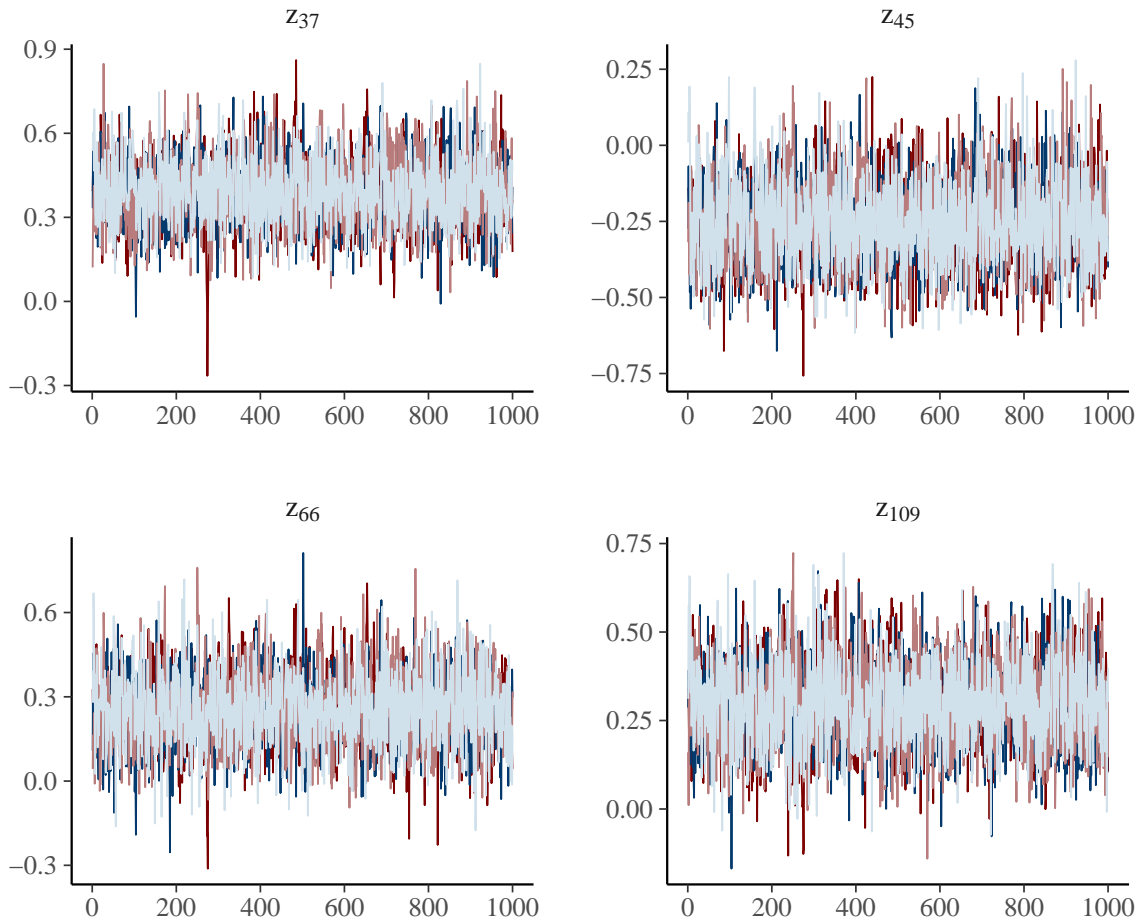


Figure A.22: Traceplots of randomly chosen random effects from the DAGAR model fitted to the areal data.

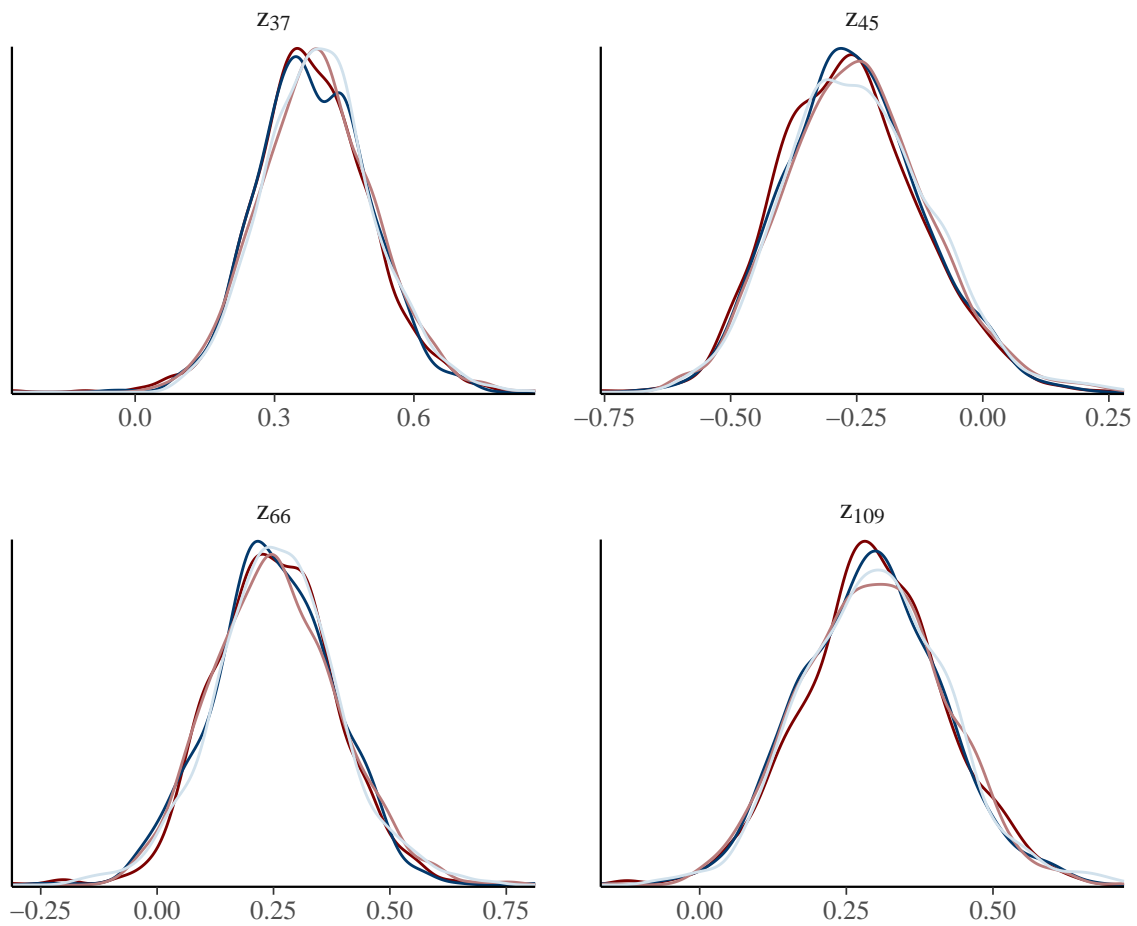


Figure A.23: Estimated densities of randomly chosen random effects from the DAGAR model fitted to the areal data.

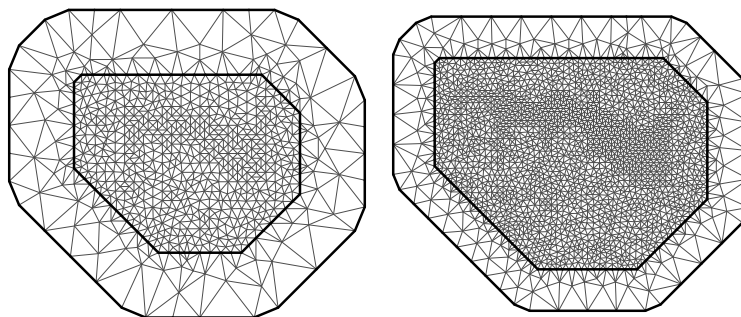


Figure A.24: The sparse and the fine meshes used in the air pollution application on the left and right side of the panel, respectively.

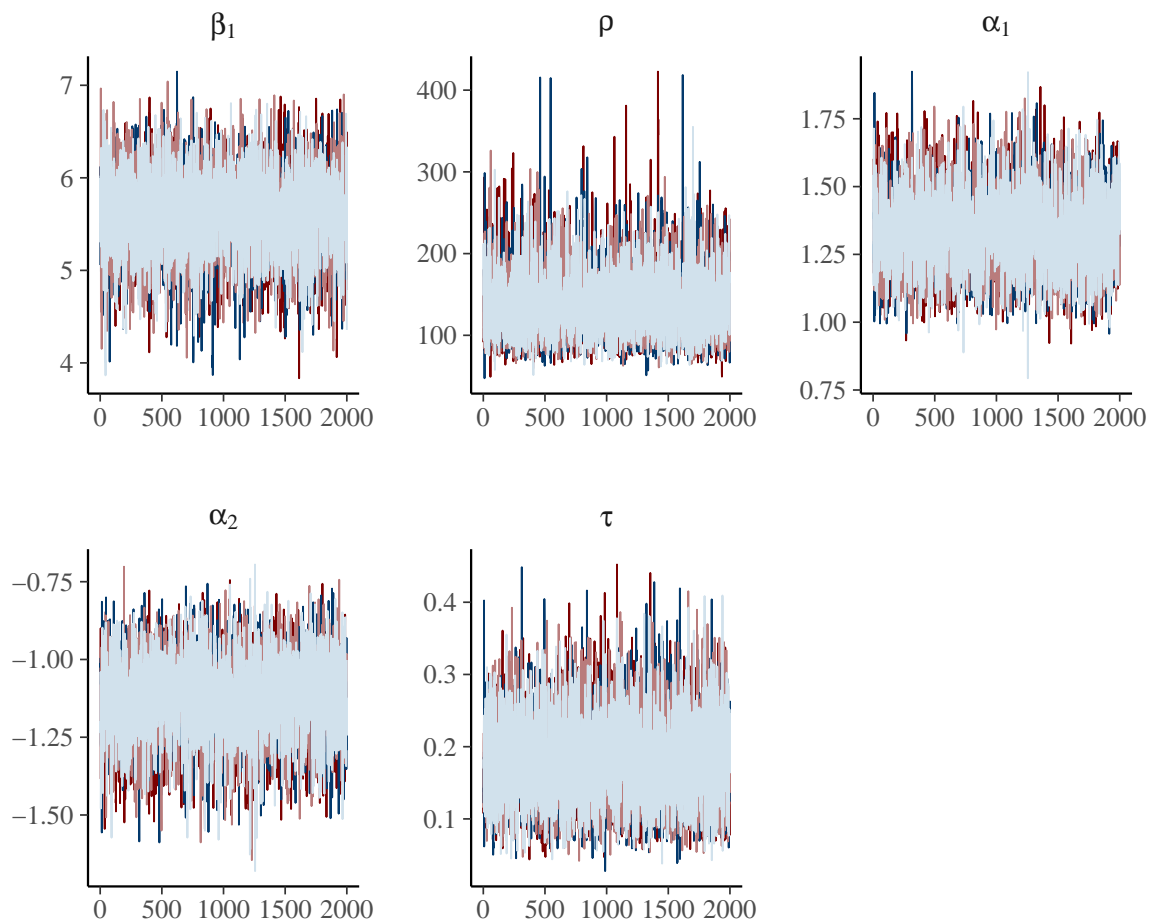


Figure A.25: Traceplots of the parameters associated to the HGP model fitted to the fused data.

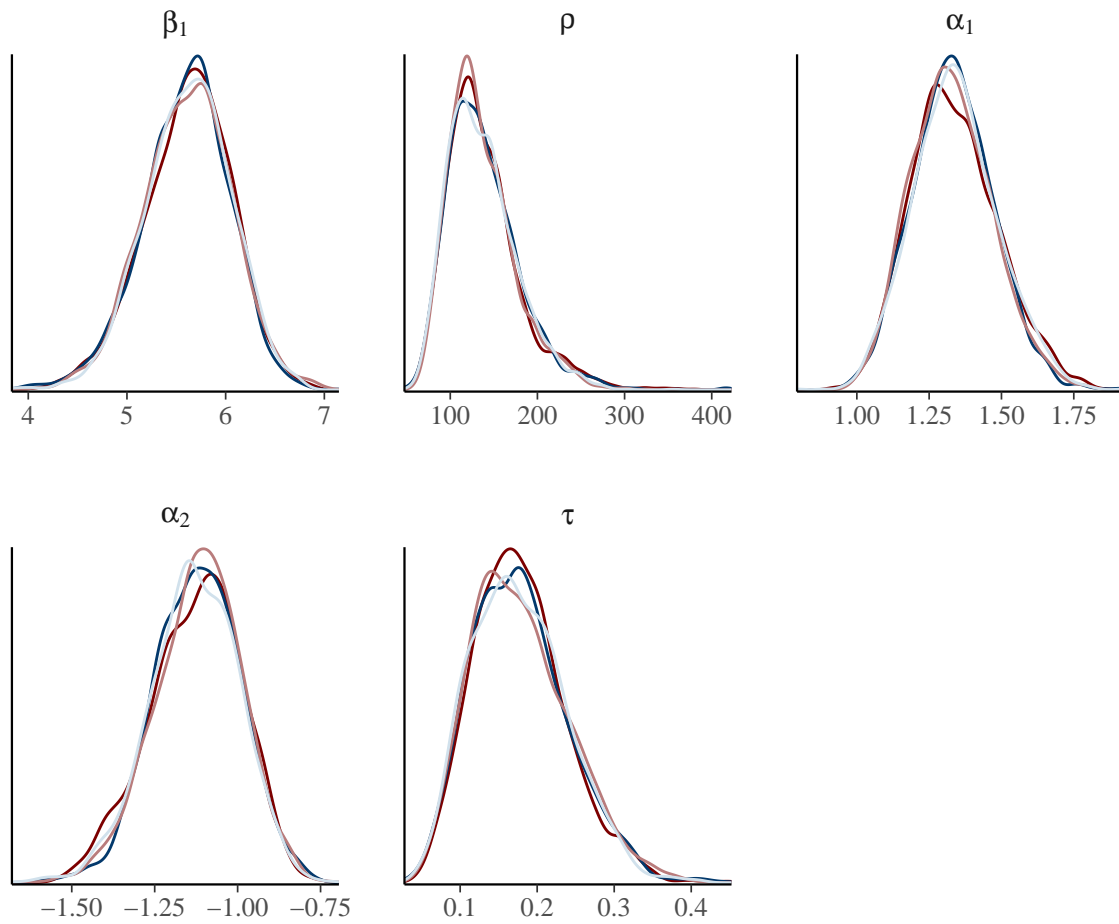


Figure A.26: Estimated densities of the parameters associated to the HGP model fitted to the fused data.